

# Lyman- $\alpha$ Emission From Cosmic Structure I: Fluorescence

Juna A. Kollmeier <sup>1</sup>, Zheng Zheng <sup>2,3</sup>, Romeel Davé <sup>4</sup>, Andrew Gould <sup>5</sup>, Neal Katz <sup>6</sup>,  
Jordi Miralda-Escudé <sup>7,8</sup>, & David H. Weinberg <sup>5</sup>

## ABSTRACT

We present predictions for the fluorescent Ly $\alpha$  emission signature arising from photoionized, optically thick structures in Smoothed Particle Hydrodynamic (SPH) cosmological simulations of a  $\Lambda$ CDM universe using a Monte Carlo Ly $\alpha$  radiative transfer code. We calculate the expected Ly $\alpha$  image and 2-dimensional spectra for gas exposed to a uniform ultraviolet ionizing background as well as gas exposed additionally to the photoionizing radiation from a local quasar, after correcting for the self-shielding of hydrogen. As a test of our numerical methods and for application to current observations, we examine simplified analytic structures that are uniformly or anisotropically illuminated. We compare these results with recent observations. We discuss future observing campaigns on large telescopes and realistic strategies for detecting fluorescence owing to the ambient metagalactic ionization and in regions close to bright quasars. While it will take hundreds of hours on the current generation of telescopes to detect fluorescence caused by the Ultraviolet Background (UVB) alone, our calculations suggest that of order ten sources of quasar-induced fluorescent Ly $\alpha$  emission should be detectable after a 10 hour exposure in a 10 arcmin<sup>2</sup> field around a bright quasar. These observations will help probe the physical conditions in the densest regions of the intergalactic medium as well as the temporal light curves and isotropy of quasar radiation.

---

<sup>1</sup>Observatories of the Carnegie Institution of Washington, 813 Santa Barbara Street, Pasadena, CA 91101

<sup>2</sup>Institute for Advanced Study, Einstein Drive, Princeton, NJ 08540

<sup>3</sup>John Bachall Fellow

<sup>4</sup>Steward Observatory/TAP, Univ. of Arizona, 933 N. Cherry Ave. Tucson, AZ 85721

<sup>5</sup>Dept. of Astronomy, The Ohio State University, 140 W. 18th Ave, Columbus, OH 43210

<sup>6</sup>Dept. of Astronomy, University of Massachusetts, Amherst, MA 01003

<sup>7</sup>Institució Catalana de Recerca i Estudis Avançats, Barcelona, Spain

<sup>8</sup>Institut de Ciències del Cosmos, Universitat de Barcelona

## 1. Introduction

A cornerstone of the current picture of galaxy formation and evolution is the existence of filaments of non-uniform gas that form the backbone of cosmic structure. The presence of this material has been inferred via neutral hydrogen absorption line studies of background quasars for nearly a half century (e.g., Bahcall & Salpeter 1965, 1966; Bahcall et al. 1966; Lynds 1971), and comparison of these types of observations with hydrodynamic cosmological simulations led to a major breakthrough in understanding how this observable material relates to the underlying dark matter distribution (Zhang et al. 1995; Miralda-Escudé et al. 1996; Hernquist et al. 1996; Hui & Gnedin 1997; Croft et al. 1998, Cen et al. 1994, Bi & Davidsen 1997). But these observations only provide information along one-dimensional (1D) lines-of-sight through the matter distribution, which is compared to similar 1D cuts through theoretical models. Owing to the rarity of close quasar pairs, information transverse to the line of sight is difficult to obtain in absorption. As a result, the 3D geometry, contents, and specific relation of intergalactic gas to galaxies remain among the most important outstanding questions in galaxy formation.

It has been long recognized that exploiting the emission in the strong  $1s - 2p$  ( $\text{Ly}\alpha$ ) transition of hydrogen could prove helpful for eventually observing the 3D intergalactic medium (IGM) *directly* (Hogan & Weymann 1987; Gould & Weinberg 1996), allowing us to test models of the structure of the IGM and determine the role of the IGM in the process of galaxy formation as well as the effects of galaxy formation on the IGM. Apart from the potential  $\text{Ly}\alpha$  emission from intergalactic stars, there are two mechanisms for generating  $\text{Ly}\alpha$  emission that dominate in the overdense regions of the intergalactic medium probed by current technologies: recombination radiation following photoionization (fluorescence) and cooling radiation. A third mechanism, scattering of photons emitted by any source and redshifted into  $\text{Ly}\alpha$  is important at low column density as discussed below. Photoionization of intergalactic neutral hydrogen followed by recombination yields fluorescent emission of  $\text{Ly}\alpha$  photons from the recombining gas at an efficiency of approximately 0.66  $\text{Ly}\alpha$  photons for each ionizing photon (Osterbrock 1962; Spitzer 1978; Gould & Weinberg 1996). The ionizing radiation that keeps the  $\text{Ly}\alpha$  forest highly ionized (the metagalactic ultra-violet background (UVB)) probably originates from galaxies and quasars. Some of these sources are very luminous, implying large-scale fluctuations in the radiation intensity. Another important source of intergalactic  $\text{Ly}\alpha$  emission is cooling radiation. As gas settles into galactic potential wells, it radiates its gravitational potential energy, and a significant fraction of this energy emerges in the  $\text{Ly}\alpha$  line because much of the cooling gas has temperature  $T \sim 10^4 - 10^5$  K even when the halo virial temperature is higher (Binney 1977; Katz 1992; Fardal et al. 2001; Haiman et al. 2000). Fluorescence stimulated by the UVB, fluorescence stimulated by local sources (e.g., nearby quasars), and cooling radiation all have potential to reveal the

structure of the IGM and the mechanisms of gas accretion by forming galaxies.

The original predictions for the fluorescent Ly $\alpha$  emission signal from the uniform UVB concluded that it is faint, requiring many hours of integration on 10m class telescopes even with optimistic assumptions for the UV background radiation field (e.g., Gould & Weinberg 1996). These studies indicated that if one is searching for the fluorescence signature from the UVB alone, only optically thick systems, corresponding to dense patches of the IGM or the outer regions of galaxies, could be realistically probed with current technology. Here “optically thick” refers to the Lyman continuum, implying neutral hydrogen column densities in excess of  $2 \times 10^{17} \text{cm}^{-2}$ . An optically thick cloud, in the absence of all ionizing sources except the photoionization from a uniform UVB, should glow with a maximum surface brightness of roughly 50% of the intensity of the ionizing background (or approximately  $1.4 \times 10^{-19} [(1+z)/3]^{-4} \text{erg s}^{-1} \text{cm}^{-2} \text{arcsec}^{-2}$ ). Precise measurements of this signal can probe the actual *value* of the UVB itself, and the large  $O(100 \text{ hour})$  programs that are necessary to reach this low signal level are currently underway but have yet to reach these faint levels (e.g., Rauch et al. 2008).

A substantially enhanced Ly $\alpha$  surface brightness may be produced, however, in optically thick systems in the vicinity of luminous sources that increase their rate of recombinations and Ly $\alpha$  emission when they are exposed to the radiation of a local source. There is good reason to search for the glow of Lyman limit systems near the most luminous quasars, which could be detected in much less observing time than the glow owing to the metagalactic background. These observations may reveal the masses, sizes, and kinematics of the absorption systems.

Recent observations have discovered significant numbers of extended “Ly $\alpha$  blobs” whose sizes and surface brightnesses demand explanation (e.g., Steidel et al. 2000; Matsuda et al. 2006; Dey et al. 2005) and seem too large to be consistent with Ly $\alpha$  emission from star formation alone. To interpret the results from increasingly larger samples of observed extended Ly $\alpha$  emission, accurate predictions for the Ly $\alpha$  emission signal from the processes described above are necessary to understand the physical origin of the luminosity of these systems. Furthermore, as increasingly ambitious surveys are planned to look for this faint emission, it is important to have accurate theoretical expectations from which these surveys can optimize their observing strategy and telescope resources.

Because Ly $\alpha$  is a resonant line, it is non-trivial to estimate the detailed Ly $\alpha$  emission from cosmological simulations. Fluorescent Ly $\alpha$  photons are typically generated at an ionizing optical depth,  $\tau_{\text{ion}} \sim 1$ . This optical depth corresponds to  $\tau_{\text{Ly}\alpha} \sim 10^4$  at the Ly $\alpha$  line center, for a typical temperature of  $\sim 10^4 \text{K}$ . Therefore, the photon will be absorbed and re-emitted a number  $\tau_{\text{Ly}\alpha} \sim 10^4$  times, undergoing a random walk in frequency until it is

scattered into the line wing by a high-velocity atom, where the optical depth is of order unity, at which point the photon can emerge from the gas toward the observer. Simulating the Ly $\alpha$  emission signature, therefore, requires computationally expensive radiative transfer calculations that cannot currently be performed self-consistently at runtime in cosmological simulations. Zheng & Miralda-Escudé (2002a) (hereafter ZM02) demonstrated that one can obtain accurate line-transfer results by employing a Monte Carlo technique. This technique makes it possible to predict Ly $\alpha$  emission from arbitrary gas-density, temperature, and velocity distributions.

In this work, we combine the Monte Carlo line transfer method with the outputs of large-scale hydrodynamic simulations and examine the Ly $\alpha$  emergent from structures that form in an  $\Lambda$ CDM universe. In Paper I we focus on fluorescent Ly $\alpha$  from the uniform UVB and also from local ionizing sources. We will address cooling radiation in Paper II (Kollmeier et. al, in preparation) and will refer to it here only briefly. These computations have two objectives: 1) to allow a comparison of simulations with observations, which will reveal successes and failures of the treatment of gas physics in the current generation of hydrodynamic cosmological models and 2) to serve as a guide to future large observational programs by providing theoretical benchmarks from specific simulations.

Several studies have improved on the predictions of Gould & Weinberg (1996) and have analyzed the Ly $\alpha$  emission signature from cosmological simulations without including detailed line radiative transfer (Fardal et al. 2001; Furlanetto et al. 2005). More recently, several authors have used the method of ZM02 to include line transfer for a variety of applications ranging from fluorescence (Cantalupo et al. 2005) to cooling radiation (Dijkstra et al. 2006a) to Ly $\alpha$  emitters (Dijkstra et al. 2006b; Hansen & Oh 2006; Tasitsiomi 2006)

For purposes of this paper we *define* fluorescent Ly $\alpha$  emission to be that produced by recombinations that directly follow photoionizations by the UVB or a quasar source. Specifically, this means that the fluorescent emissivity of a gas element is 0.66 times its photoionization rate (Osterbrock 1962; Spitzer 1978). Although the observations cannot tag photons separately as fluorescent emission and cooling radiation, we treat them separately in our studies for two reasons. First, they are physically distinct mechanisms, and it is interesting to investigate them separately and see whether they have different observational signatures (source sizes, velocity widths, etc.). Second, the cooling radiation predictions are sensitive to the gas temperatures, and the simulations do not compute these self-consistently because they do not include self-shielding during dynamical evolution. We will devote considerable attention in the next paper in this series to correcting the gas temperatures for self-shielding and to understanding the sensitivity of the cooling radiation predictions to these corrections, but here we circumvent the issue by focusing on fluorescent emission alone. We still have

to worry about the effect of gas temperature on neutral fractions, but the effect is smaller and we discuss this in Appendix C. Finally, we note that photoionization also induces Ly $\alpha$  emission by *heating* the gas, and that this effect is similar in magnitude to the direct recombinations. We also treat the Ly $\alpha$  emission induced by photoionization heating as cooling radiation.

Finally, the third process of scattered Ly $\alpha$  photons from all distant sources becomes important at low column densities in the Ly $\alpha$  forest. Continuum photons emitted between Ly $\alpha$  and Ly $\beta$  can be scattered when they are redshifted to the Ly $\alpha$  resonance line. The brightness of this scattered Ly $\alpha$  emission relative to the fluorescent Ly $\alpha$  emission discussed here can be easily computed in the limit when both the Ly $\alpha$  optical depth,  $\tau_\alpha$ , and the optical depth at the Lyman limit,  $\tau_{LL}$ , are small. The scattered intensity  $I_s$ , compared to the fluorescent brightness,  $I_f$ , is given by

$$I_s \sim I_f \frac{J_\alpha}{J_{LL}} \frac{f_\alpha}{\bar{g}_\nu} 2(\beta + 3) \frac{\max(1, \tau_{LL})}{\max(1, \tau_\alpha)} \quad (1)$$

where  $J_\alpha$  and  $J_{LL}$  are the background intensities at the Ly $\alpha$  and Lyman limit frequencies, the spectral index of the ionizing background is  $J_\nu \sim \nu^{-\beta}$ ,  $f_\alpha = 0.416$  is the oscillator strength of Ly $\alpha$  and  $\bar{g}_\nu \simeq 0.9$  is the average Gaunt factor of the ionization cross section. The expression at the end of this equation provides a rough approximation of what is expected for the case when the optical depths are not small. The scattered radiation dominates in the Ly $\alpha$  forest, but is small when  $\tau_{LL}$  becomes close to 1 unless the decline of the background intensity from the Ly $\alpha$  to the Lyman limit frequencies is extremely large (note that  $\tau_\alpha/\tau_{LL} \sim 10^{3.5}$  for the typical Ly $\alpha$  forest velocity dispersion).

The current paper will present both our methods and our first results. We will present the results from idealized models of fluorescent gas clouds and from cosmological hydrodynamic simulations. The use of idealized models is complementary to results from hydrodynamic simulations and serves two main functions. First, we use these cases as illustrations and tests of our numerical machinery, checking that it functions properly when we have analytic results with which to compare. Second, owing to the freedom we have in modeling idealized cases, they are relevant to and can be compared with current observations of individual systems. The complementary role of the hydrodynamic simulations is to provide realistic predictions for large samples of emitters in arbitrary patches of the universe in a cosmological model. These predictions are useful for future surveys in which *ensembles* of systems are being examined.

In §2, we review the method developed in ZM02 and describe how we adapt their algorithm to work in conjunction with generalized particle distributions, and with the output of smoothed particle hydrodynamic (SPH) cosmological simulations in particular. We present

our results for the Ly $\alpha$  emission signature from a simple spherical geometry in §3 and for two cosmological simulations in §4. We discuss these results in the context of currently available observational facilities and recent observations in §5. We summarize our results and present our conclusions in §6. For the interested reader, we provide more information about the computations carried out in this study in the Appendices.

## 2. Method

### 2.1. Overview of Machinery

The machinery we develop includes three parts. First, we apply self-shielding corrections given the distribution of SPH particles, either from the output of cosmological simulations or from model structures. Then, the distributions of gas density, temperature, velocity, and emissivity, represented by SPH particles, are put onto a grid. Finally, we apply the Monte Carlo Ly $\alpha$  radiative transfer algorithm of ZM02 to the grid and obtain Ly $\alpha$  images and spectra. The ZM02 algorithm can be applied to systems with arbitrary geometry and arbitrary distributions of gas density, temperature, and velocity. It is modified to work in conjunction with the gas distribution prepared by the first two parts of the machinery. We give a brief review of the ZM02 algorithm below and describe the first two parts of the machinery in detail in the next two subsections.

In the ZM02 Monte Carlo algorithm, for each photon, the scattering process is generally described by three steps: 1) the initial position of each Ly $\alpha$  photon is generated based upon the emissivity distribution in the gas while its initial direction is randomly drawn; 2) the optical depth,  $\tau$ , through which the photon will travel before scattering is drawn from an exponential distribution  $\exp(-\tau)$ , and the spatial location for the scattering at this optical depth is determined along the initial direction from the neutral hydrogen distribution (density, temperature, and velocity) and the scattering cross section; 3) the thermal velocity of the scattering atom is determined, and the new frequency and direction of the photon are calculated. In general, we use the term “scattering” to refer to this process of absorption and re-emission. In the rest frame of the absorbing atom, the Ly $\alpha$  photon is re-emitted with an unchanged frequency, except for the recoil effect (which the code accounts for but is negligibly small for our applications). The calculation of scattering is performed in the restframe of the atom and the frequency and direction of the scattered photon are transferred back to the laboratory frame. When calculating the photon free path, the bulk motion (fluid velocity) of the medium is taken into account by using the frequency in the fluid frame to compute the (thermally broadened) scattering cross section. With the new frequency and direction, steps 2) and 3) are repeated until the photon escapes the system.

To generate the image of the Ly $\alpha$  emission, a fixed direction of observation is chosen, and the output of the computation is stored in a 3D array containing the observed Ly $\alpha$  spectrum at each projected spatial position. At each photon scattering, the probability that the photon escapes along the chosen direction of observation is calculated, and this probability is added to the pixel in the 3D array corresponding to the projected position and frequency of the photon. The scattering of Ly $\alpha$  photons can be divided into two regimes. Around the line center, the scattering cross section has a thermal core with high amplitude, and at large frequency offsets, the cross section follows the Lorentz wing. For Ly $\alpha$  scatterings in a medium with high optical depth, the frequency of a Ly $\alpha$  photon changes back and forth around the line center (“core” scatterings) with little change in its spatial position, until it suffers a scattering that leads to a large frequency jump that shifts it out of the core regime. To avoid spending excessive computational time performing the core scatterings with little spatial diffusion, we introduce a numerical acceleration scheme to skip the core scatterings. In the fluid frame, if the absolute value of the frequency offset from the line center  $\nu_0$  is within  $q$  times  $(\sigma/c)\nu_0$  before scattering, where  $\sigma$  is the 1D thermal velocity dispersion of the hydrogen atoms and  $q$  is a positive number, we draw a frequency offset directly from a distribution to assign the frequency after scattering. This distribution is a Gaussian distribution of width  $(\sigma/c)\nu_0$  with the central  $\pm q(\sigma/c)\nu_0$  part excluded. The photon then travels with this new frequency until the next scattering. In our applications, the acceleration scheme is invoked only if the line-center optical depth across the grid cell (see §2.3) exceeds  $10^3$ . We take  $q = 3$  and find that choosing it to be smaller does not affect the final spectra. We also tested the using the acceleration scheme advocated by Tasitsiomi (2006), which assumes an optical-depth dependent core width. We find that adopting that scheme does not have noticeable effects in the results of our application here, and we therefore use our constant core width approach.

As discussed in §1, we apply our machinery to analytically specified, isolated gas clouds and to gas distributions extracted from SPH simulations. The only difference between our two configurations (in terms of code operation) is the setup of the gas particle properties. Once these are determined from the cosmological or analytic density field, we proceed in exactly the same manner for both cases. We describe our procedure for determining the gas properties below.

## 2.2. SPH Particles and the Self-Shielding Correction

In the SPH technique, the density field is represented by discrete particles with an extent determined by a 3D kernel or smoothing length (Monaghan & Lattanzio 1985). The

smoothing lengths of the particles are chosen to overlap a fixed number of particles to ensure accurate representation of the fluid. Each particle has an associated temperature and velocity that capture the (continuous) properties of the fluid.

In our cosmological SPH simulation, particles are exposed to a uniform photoionizing background in the approximation that all of the gas is optically thin (Katz et al. 1996). In reality, however, some of the gas is optically thick and should be self-shielded. Accounting for the self-shielding effect is particularly important for the Ly $\alpha$  emission signature, a signature that critically depends on the recombination rate and, therefore, on the distribution of ionized and neutral gas. We introduce an algorithm to perform the self-shielding correction *a posteriori* to the neutral fractions of particles of gas experiencing illumination by either the uniform UV background or a local ionizing source.

We note that because of this self-shielding correction, if simulation temperatures were directly adopted, they would also be too high in general, but specifically in dense regions. We make the following correction for this effect: for particles with hydrogen number densities  $n_H > 1 \times 10^{-3} \text{ cm}^{-3}$  and temperatures  $T < 5 \times 10^4 \text{ K}$ , we set the particle temperature to  $T_{\text{corr}} = 10^4 \text{ K}$ . Particles with temperatures in excess of  $T = 5 \times 10^4 \text{ K}$  have been shock-heated, and these high temperatures are thought to be more robust, so we do not modify them. We calculate neutral fractions using these revised temperatures including photo- and collisional ionization of the gas. We do not alter the simulation temperatures when running the scattering calculation. We discuss the effects of adopting the simulation temperatures directly in Appendix C. The self-shielding correction is performed directly on the particles, rather than on a grid, to retain the full resolution in the SPH gas distribution.

For all of our calculations we adopt a power-law spectrum for the ionizing background. To make predictions for fluorescence in the presence of both the UVB and a local ionizing source, we have run additional cases in which we have placed a bright quasar at different locations relative to the gas distribution. We assume the quasar also has a power-law ionizing spectrum and emits isotropically.

We correct for the effect of self-shielding on a particle-by-particle basis by computing for each particle the optical depth contributed by all particles that lie within 3 smoothing lengths,  $h_s$ , of the sightline from each particle along the 6 principal directions ( $\pm x, \pm y$  and  $\pm z$ ) of the box (plus the additional quasar direction when the quasar is present). For computational convenience, we use the equivalent Gaussian form of the kernel for our calculations, however the simulation is run with a cubic spline kernel. The contribution of a particle's density to the optical depth outside of 3 smoothing lengths is negligible. Because we are primarily interested in the transition layers between optically thick and thin regimes in a given structure, we must further correct the optical depth to account for the density gradient



across a particle. We describe our procedure and tests for this in detail in Appendix A for the interested reader; including the density gradient makes a critical difference to the accuracy of the result. The average of the attenuated UVB intensity over the six directions is adopted as the mean intensity at the center of the particle. At this position, the neutral hydrogen fraction is determined through photoionization equilibrium. For the case of illumination by a quasar, which can be put at any reasonable position, the attenuated ionizing flux from the quasar’s direction is also calculated and added to the photoionization term for the neutral hydrogen determination. Since each particle’s neutral fraction changes via this procedure, we carry it out iteratively until achieving a fractional convergence of  $10^{-2}$  between the old and new neutral fractions for the most discrepant particle in the region. The code for the self-shielding correction can thus deal with the general case of photoionization from UVB and/or a local ionizing source.

For particles with ionizing  $\tau \sim 1$  we are particularly sensitive to the resolution of our underlying simulation. We correct the optical depths for particles as described in Appendix A. This correction ensures an accurate representation of both the density field and the neutral fractions of particles throughout the box. However, in the case of quasar-induced illumination, the resolution of our simulations is simply not sufficient as detailed in Appendix A. These calculations should be regarded as lower limits to the possible detectable emission. For the purposes of applying the Ly $\alpha$  transfer code, we represent the corrected gas distributions from particles with a regular grid as we describe below.

### 2.3. From Particles to a Grid

To conveniently apply the scattering code, we resample the SPH output at a fixed redshift onto a 3-dimensional grid. In each grid cell, the quantities to be determined from the particle distribution are the neutral hydrogen density, the emissivity, the temperature, and the fluid velocity.

For the *neutral* density  $\rho_{\text{cell}}$  and emissivity  $\epsilon_{\text{cell}}$  in a cell, we determine the fraction of neutral mass and Ly $\alpha$  luminosity of each particle that falls into the cell according to the SPH profile of each particle and add contributions from all relevant particles. We have

$$\rho_{\text{cell}} = \frac{\sum_{i=1}^{N_p} m_{\text{neut},i} K_i}{V_{\text{cell}}} \quad (2)$$

and

$$\epsilon_{\text{cell}} = \frac{\sum_{i=1}^{N_p} l_i K_i}{V_{\text{cell}}}, \quad (3)$$

where  $N_p$  is the number of particles contributing to the cell under consideration,  $V_{\text{cell}}$  is the volume of the cell,  $m_{\text{neut},i}$  and  $l_i$  are the neutral hydrogen mass and Ly $\alpha$  luminosity of the  $i$ -th particle, and  $K_i$  is the fraction of the particle that overlaps the cell based on its SPH kernel (eq. [14] of Katz et al. 1996). The luminosity of a particle is determined from the emissivity at the particle position (defined as 0.66 times the ionization rate at the location of the particle) and its volume.

Only the distribution of neutral hydrogen is important for Ly $\alpha$  scattering. Therefore, for the temperature or fluid velocity in each cell, we calculate the neutral-mass-weighted average, that is

$$Q_{\text{cell}} = \frac{\sum_{i=1}^{N_p} m_{\text{neut},i} K_i Q_i}{\sum_{i=1}^{N_p} m_{\text{neut},i} K_i}, \quad (4)$$

where  $Q$  is either the temperature  $T$  or one of the three components ( $v_x, v_y, v_z$ ) of the bulk velocity. The bulk velocity of each particle is the sum of its peculiar and the Hubble flow velocity  $\mathbf{v}_H = H\mathbf{r}$  (referenced to the center of the box).

To perform the Ly $\alpha$  scattering calculation, we must represent the emissivity with a finite number of photons and then “launch” these photons in the gas distribution. We could do this in a variety of ways: for example, we could launch photons with a number in proportion to  $\epsilon$ , or launch a single photon per cell and weight these photons by  $\epsilon$ . We choose an intermediate course to efficiently sample the emissivity distribution while minimizing computation time. We map the emissivity,  $\epsilon$ , of a cell to the number,  $N_\gamma$ , of photons launched from the cell through the monotonic function  $G(\epsilon)$ ,

$$G(\epsilon) = \begin{cases} f\epsilon/\epsilon_{\text{crit}}, & \text{if } \epsilon/\epsilon_{\text{crit}} \leq N_{\text{tr}}, \\ fN_{\text{tr}} \log_{N_{\text{tr}}}(\epsilon/\epsilon_{\text{crit}}), & \text{if } \epsilon/\epsilon_{\text{crit}} > N_{\text{tr}}. \end{cases} \quad (5)$$

The values of  $\epsilon_{\text{crit}}$  and  $f$  determine the number of photons launched given the gas distribution and grid size. In practice, we choose  $\epsilon_{\text{crit}}$  such that we draw a sufficient number of photons for a fiducial grid resolution (e.g.  $32^3$ ) with  $f = 1$ . We scale  $f$  in proportion to the grid resolution,  $N_{\text{grid}}$ , as  $N_{\text{grid}}^{-3}$  for other resolutions. We choose  $N_{\text{tr}} = 10$  in our calculation for convenience. Adopting this scheme, the total number of photons launched from the entire grid is approximately independent of the grid resolution. We note that the 2D spatial resolution of the Ly $\alpha$  image is always matched to the the 3D resolution of the grid.

We weight the photons such that we recover the correct luminosity for each cell. The number  $N_\gamma$  of launched photons from each cell is forced to be an integer. If  $G(\epsilon) \geq 1$ , we round it to the nearest integer  $N_\gamma = [G(\epsilon)]$  and assign a weight  $\epsilon V_{\text{cell}}/N_\gamma$ . If  $G(\epsilon) < 1$  for a cell, we draw a uniform random deviate between 0 and 1. If the random deviate is greater than  $G(\epsilon)$ , no photon is launched from the cell. If it is smaller than  $G(\epsilon)$ , a single photon is

launched with a weight of  $\epsilon V_{\text{cell}}/G(\epsilon)$ . That is, for these undersampled cells [ $G(\epsilon) < 1$ ], the single photon drawn carries the luminosity corresponding to  $1/G(\epsilon)$  cells of similar emissivity.

### 3. Case I: SPH Singular Isothermal Sphere

We first turn our attention to the case of a singular isothermal sphere (SIS) in rotation represented by SPH particles. The simple case of a rotating spherical cloud can help to develop physical intuition for what we should expect for images and line profiles of fluorescent clouds. This will prove useful for studying and interpreting the more complex results from the 3D simulations.

This case has a well-understood solution and therefore acts as a benchmark test of our machinery. The SIS has the added benefit of being analogous and easily adaptable to specific high-surface-brightness configurations (e.g., a cloud irradiated by a nearby quasar) that may be observed with substantially reduced telescope time. The case of fluorescence from a singular isothermal sphere is discussed for a range of physical parameters in ZM02a, and we compare with their results as appropriate. We further anisotropically illuminate our SIS by a luminous local source (a quasar), which we will discuss in §3.2. We fix the temperature of our sphere to  $2 \times 10^4$  K, and neglect collisional ionization to compute the ionized fraction.

#### 3.1. A SIS in a Uniform UV Background

We first examine a  $z = 3$  singular isothermal sphere exposed to a uniform ionizing background. In our calculations we assume a UVB intensity of the form  $I_\nu = 3 \times 10^{-22} (\nu_L/\nu) \text{ erg s}^{-1} \text{ cm}^{-2} \text{ Hz}^{-1} \text{ sr}^{-1}$  where  $\nu_L$  is the frequency at the Lyman limit. This is close to the spectrum computed by, e.g., Haardt & Madau (1996) in shape and over the frequency range that matters, and is consistent with recent measurements of the cosmic UVB (e.g., Kirkman et al. 2005). We further assume a  $\Lambda$ CDM cosmology with Hubble constant  $H_0 = 65 \text{ km s}^{-1}$ ,  $\Omega_m = 0.3$  and  $\Omega_\Lambda = 0.7$ . The sphere has total mass of  $10^{11} M_\odot$  and a 5% gas fraction. The virial radius  $R_{\text{vir}} = 37.4 \text{ kpc}$  and virial velocity  $V_{\text{vir}} = 107 \text{ km s}^{-1}$  are set by the total halo mass (e.g., Padmanabhan 1993). The velocity dispersion (from both thermal and turbulent contributions) of the system is set to be  $51 \text{ km s}^{-1}$ . The cloud is rotating with a flat rotation curve with a circular velocity equal to  $V_c^2 = V_{\text{vir}}^2 - 2\sigma^2$ . We ignore the ellipticity this rotation would induce. We set the temperature of the sphere to be  $2 \times 10^4$  K throughout. For gas in high-density shielded regions, the cooling times are very short and the gas is likely to have the indicated low temperature given the available cooling and

heating processes. The density of the sphere is represented by particles of fixed mass and with smoothing lengths chosen to enclose 12 neighboring particles. We distribute the mass according to the SPH kernel.

As a key component, our self-shielding code should calculate the correct value for the neutral fraction of each particle. This determines the photoionization rate, and therefore, the emission rate of Ly $\alpha$  photons. In the top panel of Figure 1 we show the neutral fraction,  $X_{\text{HI}}$ , of particles in the sphere as a function of radius. The effect of self-shielding is clear in this diagram. The black points show the optically thin case, in which we have exposed each particle in the cloud to the same ionizing flux (corresponding to a photoionization rate of  $9.5 \times 10^{-13} \text{s}^{-1}$ ). The blue points show the neutral fraction of particles after we have applied our self-shielding correction. At the center of the cloud, the gas becomes completely neutral owing to the shielding layer, which is recombining rapidly enough to keep the inner cloud completely neutral: no photoionizing photons are able to penetrate to this depth. This shielding layer is very thin — it is effectively a skin of about only 2 kpc separating nearly completely ionized from completely neutral gas. It is from this thin layer, in addition to the extended emission from the larger optically thin regions, from which Ly $\alpha$  emission emerges. Our results for the “SPH” version of the singular isothermal sphere are in good agreement with the results of ZM02 (shown by the red line in the figure). Of interest for absorption line studies is the projected neutral hydrogen column density of this cloud, which is shown in the middle panel of Figure 1. If there were a quasar directly behind this system, it would be considered a Damped Ly $\alpha$  system (DLA) over the  $\sim 10$  kpc central region. We will return to this column density distribution below. The fluorescent emissivity of Ly $\alpha$  photons at each position is computed as 66% of the photoionization rate.

Once we have determined the emissivity, neutral density, temperature and velocity at each location in the gas distribution, we put these quantities on a uniform grid with length  $2R_{\text{vir}}$  on a side and run our radiative transfer code. We first ensure that our grid resolution is fine enough to resolve the self-shielding layer in our cloud. We show in the bottom panel of Figure 1 the neutral density profile of the sphere (directly from the particles) and compare it to the density profile generated from grids with resolutions of  $32^3$ ,  $64^3$ , and  $128^3$ . The SPH smoothing lengths of the particles are 0.7 kpc on average, while the smoothing length in the transition region (from optically thin to thick) is 0.25 kpc. There is a slight offset between the particle distribution and the gridded distribution, however, this is simply due to the subtle difference between the density as determined at a given particles’ position in the sphere and the density as determined from the sum of overlapping particle mass profiles. This figure demonstrates that the  $128^3$  grid recovers the density profile with sufficient accuracy for our calculations, and we adopt it for subsequent calculations of the SIS.

In Figure 2 we show the results of the radiative transfer calculation for the isothermal sphere described above. The upper left panel in this figure shows the projected Ly $\alpha$  emissivity map, which we obtain by integrating the Ly $\alpha$  emissivity along the line of sight and assuming that Ly $\alpha$  photons isotropically escape the cloud without scattering. In this sense it is a “column emissivity per solid angle” map. This emissivity image is the surface brightness one would measure if the Ly $\alpha$  photons underwent no scattering and streamed directly out of the cloud over the  $4\pi$  solid angle from where they were physically produced. This is similar to what one would observe if seeing this object in non-resonant line radiation such as H $\alpha$  or H $\beta$ , although of course these would be at much lower intensities. The lower left panel shows the emergent scattered Ly $\alpha$  image. A comparison of the true (i.e., scattered) Ly $\alpha$  image to the “column emissivity” map, illustrates the effects of spatial diffusion of the photons. Note the graininess in the Ly $\alpha$  image at low surface brightness is due to the finite number of photons we run. With respect to the emissivity map, Ly $\alpha$  emission seen in the scattered image shows spatial diffusion caused by the scattering, although the effect is small.

The right hand panels of Figure 2 show the 2D spectra of the cloud. These spectra are generated by orienting a wide slit (over the entire cloud) along the  $x$ -axis (upper-right) and  $y$ -axis (lower-right). The rotation curve for the sphere is clearly seen in the lower-right panel. Since the sphere is set to rotate around the  $x$ -axis, there is no effect of rotation in the upper-right panel, which shows the characteristic double-peaked Ly $\alpha$  profile. For clarity, we show the 1D spectrum of the whole cloud in Figure 3. The velocity profile becomes more apparent in the 1D diagram. It is clear from these figures that the photons are escaping the cloud primarily by substantial shifts from the line-center frequency, so that the scattering cross section becomes sufficiently low to allow the photon to escape. The peaks are separated by  $\approx 7 \text{ \AA}$ , which corresponds approximately to the width given by  $\pm 4\sigma \times \lambda_{\text{Ly}\alpha}/c$  where  $\sigma$  is the 1D thermal velocity dispersion (Gould & Weinberg 1996). ZM02 also present the Ly $\alpha$  images and spectrum for this case, and we find the agreement is, as expected, excellent. The brightest pixel in the Ly $\alpha$  image corresponds to a surface brightness of  $\sim 6.0 \times 10^{-20} \text{ erg s}^{-1} \text{ cm}^{-2} \text{ arcsec}^{-2}$ , which is 30% higher than expected under the “simple mirror” approximation (GW96) from our adopted ionizing background at the redshift of the SIS in the absence of heating (eq. [5] of GW96). As we show in Appendix A, this is in accordance with the expectations from an exact solution for this system based on ZM02. The excess flux over the simple mirror expectation arises from a simple limb-brightening effect. Even so, at these flux levels detecting such a system is a challenge for modern 10m-class telescopes. The maximum source surface brightness should be compared with the  $B$ -band sky brightness of  $\sim 2.9 \times 10^{-17} \text{ erg s}^{-1} \text{ cm}^{-2} \text{ arcsec}^{-2} \text{ \AA}^{-1}$ , corresponding to  $B = 22.2 \text{ mag arcsec}^{-2}$ . At the specified redshift,  $z = 3$ , this relatively bright region has size  $\sim 10 \text{ kpc}$  that would correspond to a diameter of  $\sim 1.3''$ . For our adopted UVB

at this redshift, detecting this object with a signal-to-noise ratio (S/N) of 1 would require approximately 100 hours on a 10m telescope assuming a 10 Å filter, 30% telescope efficiency and 80% atmospheric transparency. The detectability is not, however, this remote. For this calculation we have ignored two important effects: 1) heating of the gas from high-energy photoelectrons and 2) cooling radiation. We have not explicitly included the first effect in our calculation, but one can estimate its magnitude from equation (13) of GW96: it would basically double the observed surface brightness. We address the 2nd effect more completely in Paper II, as its amplitude is entirely dependent on the adopted temperature of the gas that, in this case, is physically motivated but otherwise arbitrarily chosen.

Even given more optimistic estimates for the surface brightness, it remains a major observational undertaking to detect Ly $\alpha$  emission caused by the UVB alone — for example, larger structures of size 10 arcsec<sup>2</sup> could be detected in  $\sim 26$  hours with a 10m telescope should they exist at these redshifts. More promising at present is the possibility of detecting Ly $\alpha$  emission from clouds exposed to an enhanced ionizing field. We turn our attention to this case.

### 3.2. A SIS in a Quasar Radiation Field

We now investigate the case of a singular isothermal cloud, constructed as described above, that is irradiated by a local bright quasar. The UVB + quasar case is of particular interest because of the potential surface brightness enhancement and therefore detectability of these systems. It is timely to analyze this case because of the recent detection of Ly $\alpha$  fluorescence in a DLA system irradiated by a bright quasar (Adelberger et al. 2006). As noted previously, our code for performing the self-shielding correction is equipped to deal with an anisotropic radiation field to study anisotropically irradiated gas fields, novel with respect to the cases studied in ZM02. We place the quasar at  $(x, y, z) = (-500, 0, 0)$  kpc (physical) from the center of the sphere. The quasar is assumed to emit isotropically and have a power-law continuum shortward of 912 Å of  $L_\nu = L_{\nu_L}(\nu/\nu_L)^\alpha$  where  $\alpha$  is taken to be  $-1.57$  in accord with observations (Telfer et al. 2002). We assume a specific 912 Å luminosity,  $L_{\nu_L}$  at the Lyman limit  $\nu_L$  of  $1.0 \times 10^{31}$  ergs<sup>-1</sup>Hz<sup>-1</sup> (Liske & Williger 2001) unless otherwise specified. When we turn on the quasar and examine the resulting neutral fraction for particles near the  $y = z = 0$  line, we see in the bottom panel of Figure 4 that the quasar has indeed ionized the outer edges of the cloud facing it as expected from this configuration. At the cloud, the quasar intensity corresponds to an enhancement in ionizing photon flux per unit area above the UVB of approximately 60.

In the top panel of Figure 4 we show a particle representation of the cloud near the

$z = 0$  plane, where particles are color coded according to their relative neutral fractions, i.e., their neutral fractions in the presence of the quasar relative to their neutral fractions when exposed to the UVB alone. The blue points in the diagram show those particles that have been most strongly affected by the quasar. The quasar has the most dramatic effect on the nearly neutral innermost particles and particles on direct sightlines to the quasar radiation. Particles on the opposite side of the cloud from the QSO experience a less dramatic reduction of their neutral fractions because the quasar radiation is attenuated or entirely blocked from view by the central optically thick structure. The half moon illumination caused by the quasar is apparent from this figure. In fact, it looks more like a keyhole, but the highly ionized outer layers of the cloud contribute very little to the Ly $\alpha$  surface brightness owing to their low density. We now explore how this translates into Ly $\alpha$  emissivity and, ultimately, scattered radiation.

Based on the properties of the quasar, we can determine order-of-magnitude expectations for the surface brightness of Ly $\alpha$  emission for the case in which the DLA acts simply as a “mirror”, converting 66% of the quasar’s ionizing radiation into Ly $\alpha$  fluorescence<sup>9</sup>. At the distance of the cloud, these photons should emerge as:

$$\Gamma_{\text{mirror}} = \frac{0.66 r_{SS}^2 \dot{N}_{\text{ionizing}}}{4d_q^2}, \quad (6)$$

$$\dot{N}_{\text{ionizing}} = \int_{\nu_L}^{\infty} \frac{L_\nu}{h\nu} d\nu, \quad (7)$$

Where  $r_{SS}$  is the self-shielding radius of the cloud,  $d_q$  is the cloud-quasar distance, The prefactor of 0.66 comes from the fraction of ionizing photons that eventually cascade to the Ly $\alpha$  transition (Gould & Weinberg 1996, GW96). For the systems we examine,  $d_q$  is 500 kpc and  $r_{SS}$  depends on the quasar flux as we show below. For the quasar spectrum we adopt, the peak surface brightness should go roughly as  $\sim 1.01 \times 10^{-17} [(1+z)/4]^{-4} [L_{\nu_L,31}] [d_q/(500 \text{ kpc})]^{-2} \text{erg s}^{-1} \text{cm}^{-2} \text{arcsec}^{-2}$  where  $L_{\nu_L,31}$  is the quasar luminosity at the Lyman limit in units of  $10^{31} \text{ergs}^{-1} \text{Hz}^{-1}$ . Figure 5 shows the Ly $\alpha$  images and spectra when we include the radiation field of the quasar. We see in the upper left hand panel that the effect of the quasar on the Ly $\alpha$  emission is to produce a half-moon region of high surface brightness gas. The half-moon illumination reflects the higher ionization rate and, therefore, a higher recombination rate in the portion of the cloud facing the quasar. This should be compared with the uniform emission shown in Figure 2 for the case in which the

---

<sup>9</sup>We use the term “mirror” to mean an optically thick surface that converts 66% of impinging ionizing photons to the Ly $\alpha$  frequency and re-emits these photons at a random angle.

only source of illumination is the UVB. In the Ly $\alpha$  image itself, this half-moon shape is preserved. Such a feature serves as a diagnostic of this configuration because it implies either a specially arranged gas density distribution, or an anisotropic illumination similar to the case discussed here. The spectra are also modified in the presence of the quasar. The amplitude of emission is higher as expected, and the peak separation is smaller than the case with UVB illumination alone.

The brightest feature in the QSO-irradiated cloud is 53 times brighter than the brightest feature seen from exposure to the UVB alone. The quasar itself contributes  $\sim 200$  times more ionizing flux than the UVB alone at the center of the cloud. Since the UV-absorbing and Ly $\alpha$ -emitting surface is finite and curved, as opposed to an infinite flat surface, Ly $\alpha$  photons are emitted into  $2\pi - 4\pi$  steradians. This geometric effect leads to a factor of 2-4 reduction in the surface brightness with respect to the expectation from an infinite flat “mirror”. The calculated increased surface brightness relative to the UVB-only case is in line with this expectation, given the strength of the quasar radiation field. As we show in Appendix A, the reason for any small discrepancy is that the neutral fraction profile is not being faithfully represented in our 100,000 particle case. When we run this case with 500,000 particles, we get closer to the expected value, but even this is not fully adequate. Since high-resolution cosmological simulations typically have at most 1,000,000 particles in their most well-resolved structures, current SPH simulations are simply unable to faithfully capture the steep transition from optically thick to thin that occurs in these systems. In the limit of a very bright quasar, this half-moon shape is eliminated as the ionizing flux propagates further into the cloud. We illustrate this effect in Figure 6 in which we show a sequence of surface brightness and neutral column density images as the quasar luminosity  $L_{\nu_L}$  at the Lyman limit is increased from 0 (the UVB-only case) in the left-most panel, and then from  $1.02 \times 10^{29}$  to  $1.02 \times 10^{32}$  erg s $^{-1}$ Hz $^{-1}$ . We show the impact of the quasar on the projected neutral column density of the system in the bottom panels of Figure 6. The sequence of neutral column density shows that, as expected, the neutral layers are progressively blasted away, leaving only a very small, dense core in the case of very strong quasar illumination.

There are three features to note in these figures that, in conjunction, can provide constraints on the physical situation of individual optically thick systems when observed. The first is simply the Ly $\alpha$  surface brightness. Given the quasar luminosity and distance, it is straightforward to calculate how bright (in the absence of dust) the optically thick cloud will glow. Depending on the impinging flux, this anisotropic illumination will create a half-moon or a “pac-man” type structure. The second is the frequency distribution of the photons. Most importantly, fluorescence will manifest itself as a double peaked profile with a peak separation approximately equal to  $8\sigma$  where  $\sigma$  is the cloud’s velocity dispersion, as demonstrated here. In the absence of other bulk flows, the peak separation, together with an



estimate of the object’s size, directly constrains the mass of the object. Rotation within the cloud will be apparent in the spectrum depending on the orientation of the slit to the rotation axis of the cloud. In the case we show in Figure 5, a “double” rotation curve can be clearly seen in the 2D Ly $\alpha$  spectrum. The third diagnostic is the size of the “absorber”. For a given impinging flux, halo mass, and density profile, there is a specific size over which the cloud will appear as a LLS or DLA. Combining emission observations with absorption line studies to measure the column density, one can set limits on this size and thereby set constraints on simple models such as those presented here. In §5, we demonstrate how these diagnostics work together by comparing these simple models in detail to a recently discovered system (Adelberger et al. 2006).

#### 4. Case II: A Cosmological Volume

We now turn our attention from simplified cases with well-understood geometries to predictions for the variety of structures produced in cosmological hydrodynamic simulations. For this work, we use two cosmological simulations that have complementary strengths. Our primary simulation is a  $5.555 h^{-1}$  Mpc (comoving) box at  $z = 3$  with cosmological parameters  $\Omega_m = 0.4, \Omega_\Lambda = 0.6, \Omega_b = 0.0473, \sigma_8 = 0.8, H_0 = 100h \text{ km s}^{-1} \text{ Mpc}^{-1}$  with  $h = 0.65$  (hereafter L5). The simulation has  $128^3$  dark matter and  $128^3$  gas particles and the gravitational forces are softened using a cubic spline kernel with radius of  $1.25 h^{-1}$  kpc (comoving). The mass per gas particle in the simulation is  $1.7 \times 10^6 M_\odot$ . We supplement this box with a second larger, but lower resolution, box of  $22.222 h^{-1}$  Mpc (comoving) at  $z = 2$  with the same cosmology and the same number of particles (hereafter L22). The softening radius and mass resolution for the L22 box are exactly 4 and 64 times larger than in the L5 box respectively. We use the lower-resolution simulation primarily to illustrate the redshift dependence of the Ly $\alpha$  emission signature in amplitude and morphology.

The simulations make use of the parallel version of TREEsph (Hernquist & Katz 1989; Katz et al. 1996, 1999; Dave et al. 1997) that combines smoothed particle hydrodynamics (Lucy 1977; Gingold & Monaghan 1977) and a hierarchical tree algorithm for the computation of gravitational forces (Barnes & Hut 1986; Hernquist 1987). The calculation is described extensively in Katz et al. (1996) and Kereš et al. (2005), and we refer the interested reader to that work for more details.

#### 4.1. Large Scale Structure in the UVB

We have selected a 1.5 Mpc (physical) region and a smaller 200 kpc (physical) region from the L5 simulation as well as a 1.8 Mpc (physical) region from the L22 simulation for which we make predictions for fluorescent Ly $\alpha$  emission. We show the total gas density and temperature from these simulations in Figure 7. Irradiating these gas structures with a uniform ionizing background<sup>10</sup>, we determine the neutral fractions for all of the particles within these sub-regions of the simulations using the well-tested algorithms of our self-shielding correction, which we describe in §2.2. Since we now have an arbitrary geometry and gas density distribution, we can only compare our particle neutral fractions before and after we correct them for the effects of self-shielding: we do not have a simple reference such as a self-shielding radius. We show in Figure 8 the resultant neutral fraction distribution after we perform the self-shielding correction on the SPH particles compared to the case in which all particles are exposed to a uniform UVB for the L5 simulation. The effect of the self-shielding is seen clearly by the shift toward higher neutral fractions in dense regions, with a substantial number of particles becoming completely neutral. We note that there is almost no change in the low density regions that are optically-thin to Ly $\alpha$ .

To preserve the high resolution achievable with SPH simulations, we would ideally have grid sizes that were smaller than the smallest smoothing lengths in the box. The smallest physical scale resolved in this simulation (i.e., the smallest particle smoothing length) is 0.07[0.38] kpc for the L5[L22] simulation. For a 1.5[1.8] Mpc region, this would correspond to an unrealistically high resolution grid of  $(2.1 \times 10^4)^3 [(4.7 \times 10^3)^3]$  cells. However, because they are shielded, extremely dense regions play no role in generating photons, and the requirement of grid resolution should be much less stringent in these regions. For our applications, the boundaries of any dense region will simply act as “mirrors” for the incoming photons. We, therefore, need to resolve dense regions as a whole, not individual particles inside them. We have tested the effect of grid resolution and based upon these experiments, have adopted a resolution of  $300^3$  cells (corresponding to 5kpc and 6kpc spatial resolution for the large regions of the L5 and L22 boxes respectively) to make our predictions. We adopt a spatial resolution of  $128^3$  cells (corresponding to 1.6kpc resolution) for the small sub-sub region of the L5 box. The details of these tests can be found in Appendix B.

We first examine the 200 kpc sub-sub region of the L5 simulation that contains multiple optically-thick structures. To explicitly examine the effect of frequency diffusion, we generate a Ly $\alpha$  map with the radiative transfer turned *off*, which is the same as the emissivity map.

---

<sup>10</sup>We adopt the same UVB for  $z = 2$  and  $z = 3$ . The UVB is not expected to vary significantly between these epochs (Haardt & Madau 1996)

The top panels of Figure 9 show the unscattered Ly $\alpha$  image and 2D spectrum extracted along the  $y$ -direction. The bottom panels in this figure show the image and spectrum from the full radiative transfer calculation. The connection between gas density and emission is striking in this zoomed region as one can see by comparing the upper left panel of Figure 7 with the Ly $\alpha$  image in the bottom left panel of Figure 9. Very dense knots of gas produce a substantially higher emission signature in both images and spectra.

A comparison of the top and bottom panels of Figure 9 directly shows the effect of the resonant scattering. The image in the scattered case is smeared compared to the non-scattered case owing to the spatial diffusion of the photons. The differences between these images shows the modest amount of spatial diffusion that occurs in these systems. The comparison between the 2D spectra for both cases shows that photons diffuse primarily in frequency space, in contrast to a spatial random walk. In the non-scattered image, each blob gives rise to a narrow bright line near line-center in the 2D spectrum in contrast to the characteristic broad double-peaked line profiles. The peculiar velocity and Hubble flow in the gas cause frequency shifts away from zero. When we examine the scattered image, however, we see that each structure now gives rise to a more diffuse line profile in frequency. While this realistic case is more complex than the idealized cases presented in §3, we can still see the fingerprints of resonant scattering on this scale. With the appropriate scaling, the top panel of Figure 9 could represent an image in an optically thin recombination line such as H $\alpha$ . Taking the ratio of the top and bottom panels yields an estimate of the relative morphology for lines that are optically thin and thick, respectively. While in high-emissivity locations, the difference is modest, in low-emissivity regions the difference between, e.g. an H $\alpha$  image and a Ly $\alpha$  image would be quite substantial.

We now examine the larger regions of the L5 and L22 simulations in which blobs of the size shown in Figure 9 are only a small portion. We show in Figure 10 the Ly $\alpha$  images and 2D spectra generated from the large L5 and L22 simulation regions shown in Figure 7 (with different surface brightness scale). We show the results for both simulation boxes in Figure 10 to facilitate comparison between the  $z = 2$  (top panels) and  $z = 3$  (bottom panels) cases from the L22 and L5 simulations, respectively. In contrast to the isothermal-sphere case and owing to the highly disturbed gas density and velocity structure, we do not have clean diagnostics of characteristic radii and analytic expectations for the separations of spectral features. However, a comparison of the panels of Figure 10 and the bottom panels of Figure 7 shows that the emission primarily originates from dense knots of material, as one would expect, since the emission comes from the rapidly recombining skins of optically thick cores, which should occur in regions of high density. Since we have adopted the same UVB for both redshifts, the difference in emission intensity between the images is caused primarily by the cosmological surface brightness dimming, which is  $\propto (1 + z)^{-4}$ .

The 2D spectra are quite complex as can be seen in the right panels of Figure 10. As we showed in detail in Figure 9, each blob of optically thick gas gives rise to a disturbed version of the characteristic double-peaked profile. Since we have a large number of such blobs, the resultant spectra are a superposition of many of these profiles, each modified by the fluid velocity field and the geometry (e.g. the frequency distribution may not be symmetric about the line center). The profiles shift with respect to each other because of the Hubble flow and the peculiar velocity of the gas. The complex structure seen in the 2D spectra is, therefore, generically expected owing to transfer effects. It is also worth noting that, as one approaches sufficiently low surface brightness limits, the “forest” of Lyman Limit systems illuminated by the UVB emerges. That is, many systems become visible at a similar surface brightness level — once this threshold in surface brightness is achieved, the filamentary structure is evident i.e., once one LLS is observable, many others are also visible.

In Figure 11, we show several 1D spectra from blobs of gas in different regions of the structure in the L5 box. This is analogous to obtaining a narrow-band image for a particular field and follow-up spectroscopy of the identified sources. Solid lines in the figure show the post-transfer spectra and dotted lines show the “unscattered” spectra. The overall double peaks owing to the transfer of photons are clear in some cases (e.g. A3 and A1) but unlike the isothermal case, they are not symmetric owing to the bulk velocity of the gas in the simulations. While comparison of any individual system requires detailed modeling, characteristic line-widths and morphologies from large-volume calculations such as these could be derived. Observational campaigns to obtain deep narrow-band imaging and follow-up spectroscopy are currently underway and comparison with calculations such as these will prove helpful for understanding the origin of the Ly $\alpha$  emission. We discuss the requirements for observing such fields in §5.

## 4.2. Large Scale Structure in a Quasar Radiation Field

Similar to the case discussed in §3.2, we now place a bright quasar with  $L_{\nu_L} = 1.0 \times 10^{32} \text{ erg s}^{-1} \text{ Hz}^{-1}$  (10 times brighter than for the previous SIS case) in the center of our cosmological sub-regions to examine the effect on the Ly $\alpha$  emission strength and morphology and to show the expectations for observing a field containing a bright quasar. The quasar will have little effect on the emission from gas that is already highly ionized by the UVB, but will have a substantial effect on the emission from the dense optically thick clumps that are not already significantly ionized by the UVB. We see this in Figure 12 where we show the resulting Ly $\alpha$  image and 2D spectra for the L22 (top panels) and L5 (bottom panels) simulations including a quasar. Comparing with Figure 10 one can see that in the dense

knots, the emission is brighter by more than an order of magnitude relative to the UVB-only case. We note that even in the outer reaches of this system, there is a substantial *relative* increase in the surface brightness – the quasar is sufficiently powerful to reach the edges of this region.

In Figure 13 we quantify the shift to higher surface brightness in the distribution of pixels in the resulting Ly $\alpha$  map caused by the QSO illumination. In the UVB-only case, the brightest pixels were set by the intensity of the UVB. Now, the brightest pixels are determined by the quasar flux impinging on the densest regions. The faintest pixels come from low column-density material that is highly ionized. There is, therefore, little difference at low emissivities between the UVB and UVB+QSO case since these systems already emit near maximum. The brightest systems are those that are able to remain optically thick in the presence of the vastly increased ionizing flux of the quasar. The UV photon enhancement caused by the additional ionizing flux of the quasar is  $\approx 500(d_q/1\text{Mpc})^{-2}$ . In our calculations, the brightest pixel is now  $\sim 2 \times 10^{-17} \text{erg s}^{-1} \text{cm}^{-2} \text{arcsec}^{-2}$ , a factor of  $\sim 400$  over the UVB-only case. The enhancements in the average pixel surface brightness relative to the UVB-only case are shown in Figure 13. On average, the resultant enhancement over the UVB is more modest. This is due to the geometry of the emission which can result in a factor of 2-4 suppression of the expected Ly $\alpha$  surface brightness.

Most striking is that the presence of the quasar highlights the morphology of the densest knots in the large scale density distribution. This is the “meatball” topology of Ly $\alpha$  emission referred to in GW96. The quasar brings the contrast between the emission from optically thick and optically thin sources into sharp relief since only the densest knots are able to reprocess the increased ionizing radiation. The lower surface brightness material, which appears spatially extended and fluffy, becomes sinewy in the presence of the quasar. This corresponds to material that was previously partly neutral, and has become fully ionized in the quasar’s radiation field. Hence, its fluorescent emissivity has decreased since the emissivity of the gas is proportional to the photoionization rate, which is small for gas with very low neutral fractions.

The 2D spectra for the QSO case also highlights the densest systems. The brightest knots have narrower frequency distributions compared with their counterparts in the UVB-only case. The QSO has completely photoionized many low-emissivity structures, eliminating their contribution in both the image and the spectra. The highest column-density systems are relatively smaller and brighter and, because the quasar radiation has generally lowered the neutral column-density of the gas, the spectral pattern is narrower in frequency since the photons undergo smaller frequency diffusion at lower column-densities. The double-peaks of the highest density systems become much more prominent in the presence of the quasar’s

radiation. For relatively isolated blobs, one can see clearly the double-peaked spectral feature associated with the object in the 2D spectrum (e.g. the systems located at  $(X, Y) = (0.8, 0.3)$  and  $(0.8, 1.3)$ ).

Fluorescent Ly $\alpha$  emission in quasar fields should have a very different morphology as a function of luminosity compared to fluorescence from the UVB alone. Bright knots of emission from high-column density dominate over the general emission from the IGM.

## 5. Observables

We now quantify the results presented in §4 to demonstrate how such predictions can be explicitly compared with current narrow-band imaging surveys (e.g. Steidel et al. 2000; Ouchi 2005). We will first go over some analytic expectations and see how these relate to our more detailed calculations. Then we present simulated images and extract sources from those images.

### 5.1. Analytic Considerations

What are the realistic prospects for observing Ly $\alpha$  emission from the IGM from the ground and from space? A useful figure of merit is the amount of observing time required to reach a fixed S/N. We gain some insight into the practical difficulty of this problem by considering the simple mirror approximation as cast by GW96 who obtained the following expression for S/N as a function of observing time:

$$\begin{aligned}
 S/N &= \xi \frac{\Phi_{\text{obs}}}{(1+z)^{1/2}} \left[ \frac{\pi^{1/2} D^2 f T \Delta\Omega}{16(\sigma/c)\phi_{\text{sky}}\lambda_{\text{Ly}\alpha}} \right]^{1/2} & (8) \\
 &\sim 7.5 \left( \frac{1+z}{3.2} \right)^{-3.5} \left( \frac{f}{0.25} \right)^{1/2} \left( \frac{D}{10\text{m}} \right) \left( \frac{T}{20\text{hr}} \right)^{1/2} \left( \frac{\Delta\Omega}{10\text{arcsec}^2} \right)^{1/2} \left( \frac{\sigma}{35\text{km s}^{-1}} \right)^{-1/2} & (9)
 \end{aligned}$$

where  $T$  is the integration time,  $D$  is the telescope diameter,  $f$  is the telescope efficiency,  $\phi_{\text{sky}}$  is the flux from the sky,  $\Phi_{\text{obs}}$  is the source flux,  $\sigma$  is the velocity dispersion of the source,  $\xi$  is the atmospheric transmission, and  $\Delta\Omega$  is the source size. In equation (9) we have assumed  $\xi = 0.9$  and  $\phi_{\text{sky}} = 1.85 \times 10^{-2} (\gamma \text{ s}^{-1} \text{m}^{-2} \text{arcsec}^{-2} \text{\AA}^{-1})$ , corresponding to a  $B$ -band surface brightness  $B = 22.2$ . The strong  $(1+z)$  scaling in equation (9) arises from the redshift dependence of  $\Phi_{\text{obs}}$ , assuming that the UVB intensity is constant with redshift. Using their values for the ionizing background, telescope setup and source size, they inferred that the

IGM Ly $\alpha$  fluorescence from the UVB would be marginally detected in  $\sim 20$  hours.

However, this prediction may be optimistic in several respects. The lower amplitude and flatter shape of the UVB we adopt, cause our value of  $\Phi_{\text{obs}}$  to be lower than the GW96 value by a factor of 3.11, which leads to an increase in observation time by a factor of 9.7. The typical source sizes for the brightest fluorescent sources in the simulation are not  $10 \text{ arcsec}^2$ , but rather more like  $4 \text{ arcsec}^2$ , causing a factor of 2.5 increase in observing time. This already implies typical observing programs of 500 hours instead of the 20 hours GW96 obtained for marginal detection. GW96 also adopted a matched filter that is approximately 3 times narrower than even a very narrow  $10 \text{ \AA}$  filter, causing another factor of 3 increase in observing time. GW96 further assume that sources have a Gaussian profile and that observations would reach a frequency resolution of  $\sim 1 \text{ \AA}$ . These observations would be very powerful for detecting low-level Ly $\alpha$  emission. If the source sizes in our simulation and our adopted UVB intensity are correct, then, in the presence of the terrestrial night sky, it will require  $\sim 1500$  hour exposures to detect the typical sources of fluorescence from the uniform UVB with current ground based telescopes.

This probably explains why fluorescence from the general IGM has been difficult to detect with the large 100 hour programs currently completed (Rauch 2008). In space, the sky background is 1 magnitude fainter and integration times can be longer. Future dedicated space-based and ground-based facilities will be ideal for detecting the glow of the IGM. In the near term, however, observations in quasar fields where the ionizing flux can easily be 1500 times the uniform UVB are feasible in only hours on 10m class telescopes. As we showed in §4, the morphology of emission near quasars highlights the “forest” of Lyman limit systems.

We now simulate observational maps of Ly $\alpha$  fluorescent emission from our cosmological simulations.

## 5.2. Lyman $\alpha$ Maps

To mimic narrow band Ly $\alpha$  observations, we add a background of sky photons and Poisson noise to our theoretical predictions for a specific observational setup. We fix the telescope aperture, integration time, narrow band filter width and telescope efficiency to make “exposures” of our theoretical structures. We subtract the background from these frames — simply taken to be the minimum pixel count — to create “sky-subtracted” images from our predicted Ly $\alpha$  images. We then convert our image files to standard observational image format and use the Source Extractor program (Bertin & Arnouts 1996) to identify sources from our image, just as would be done for an observed narrow-band image. We use

a  $10\text{\AA}$  filter on a 10m telescope aperture with 30% efficiency and integration times of 10 and 1500 hours to generate our observed maps.

In Figures 14 and 15 we show the maps created by this procedure for our simulated results at redshifts 2 and 3 respectively. The left panels in these figures show the UVB only cases. Right panels in the figures show the case of UVB+QSO. The difficulty of observing fluorescence is clear from the top panels of these figures, which show the resulting maps after 10 hours of integration. The middle panels show 1500 hour observations and the bottom panels show the “perfect” case (equivalent to an infinite exposure time) at the same resolution as the images to assist with identifying the features. While fluorescence from the UVB alone is not observable in 10 hours, and only marginally detected after 1500 hours at  $z = 2$  and not at all at  $z = 3$ , the quasar illuminated structures glow brightly and with high significance after a single night of observation.

With minimum high-resolution volumes of  $(5.555h^{-1} \text{ Mpc})^3$  we can begin to examine the statistics of fluorescent sources in our models. Such statistics can be compared to observations from large Ly $\alpha$  surveys (e.g., Matsuda et al. 2006; Steidel et al. 2000; Cantalupo et al. 2007; Rauch 2008). We leave a more complete statistical analysis of large simulation volumes to future work, but we demonstrate here the types of measurements we can make from our simulated data. We first look at the distribution of sources from the Source Extractor software applied to the observed maps from the UVB+QSO case presented in Figures 14 and 15. Sources are defined within the SExtractor software as being  $5\text{-}\sigma$  detections.

Figures 16 and 17 present results of this analysis for the 1.5Mpc (physical) subregion of the L5 simulation, for the 10 and 1500 hour cases, respectively. The top panels in these figures show the differential distribution of sources as a function of Ly $\alpha$  flux. The bottom panels show the fluxes of identified sources as a function of radial distance from the quasar, which is located at the center of box. In the “quasar field” the distribution of fluxes is substantially skewed toward higher values, which results from the increased photoionization of optically thick systems in the sub-region.

In the 10-hour field, 10 sources are detected, with fluxes in the range  $\sim 2 \times 10^{-19} - 2 \times 10^{-18} \text{ erg s}^{-1} \text{ cm}^{-2}$ . There is only a marginal trend of flux with distance from the quasar. One might naively expect a  $d^{-2}$  falloff in flux, but sources further from the QSO can remain self-shielded to a larger radius and therefore present a larger reflecting area. For a population of isothermal spheres, like those in §3, one can show that the expected falloff in flux is  $d^{-2/3}$ , shown by the dashed line, which approximately describes the overall trend of points. Because of the smaller reflecting area of sources at smaller radii, we expect that our fixed grid resolution smears out the brightest sources near the quasar. Therefore the radial falloff may be even flatter than  $d^{-2/3}$ . Given the slowness of the radial trend, we expect observable



sources beyond the  $750h^{-1}$  kpc radius of the volume we have analyzed. The 1500-hour map contains 76 detected sources, down to fluxes  $\sim 3 \times 10^{-20} \text{ erg s}^{-1} \text{ cm}^{-2}$ , and it again shows only a weak trend of source flux with distance from the quasar.

### 5.3. A Case Study

In this section, we compare a simple model of Ly $\alpha$  fluorescence with observations to investigate the origin of the emission. Our method has already been applied to constrain the emission mechanism for emission seen in a DLA absorption trough seen in close proximity to a background quasar (a “proximate DLA” Hennawi et al. 2009) and here we show the application to a case with different geometry.

Adelberger et al. (2006) observed a DLA with column density  $N_{\text{HI}} = (2.5 \pm 0.5) \times 10^{20} \text{ cm}^{-2}$  at  $z = 2.842$  in the spectrum of a background quasar Q1549-D10. The absorber is at a projected angular separation  $\theta_Q = 49''$  (corresponding to 380 kpc) from the bright ( $G \sim 16$ ) quasar HS1549+1919, which has the same redshift as the DLA. Extended Ly $\alpha$  emission with a double-peaked spectrum is observed at  $\theta_l = 1.5''$  (corresponding to a physical size of  $\sim 11$  kpc proper) offset from the absorber. The extended Ly $\alpha$  emission region has an apparent AB magnitude of  $G = 26.8 \pm 0.2$  mag, and the line has an equivalent width of  $\Delta\lambda_{EW} = 275 \pm 75 \text{ \AA}$  in the  $G$  band, which is  $\sim 1000 \text{ \AA}$  wide. The emission line has a peak separation of  $\sim 8 \text{ \AA}$  and a line flux of  $2.1 \times 10^{-17} \text{ erg s}^{-1} \text{ cm}^{-2}$ , which yields an inferred surface brightness of  $\sim 1 \times 10^{-16} \text{ erg s}^{-1} \text{ cm}^{-2} \text{ arcsec}^{-2}$ , assuming that the emission region has diameter of  $0.5''$ . The AB magnitude at  $912 \text{ \AA}$  estimated for the foreground quasar is  $m_{912} = 16.7$ , which corresponds to a luminosity at the Lyman limit of  $L_{\nu_L} = 1.34 \times 10^{32} \text{ erg/s/Hz}$ . From these observables we can calculate the expected Ly $\alpha$  flux owing to fluorescence induced by the quasar’s impinging radiation. Recall that in the “mirror” approximation, a fraction  $\eta = 0.66$  of the ionizing photons impinging on an optically thick cloud get re-radiated as Ly $\alpha$  photons. For a given background and quasar intensity, the observed surface brightness should be given by the following expression:

$$\pi \times SB = \frac{h\nu_\alpha \eta}{(1+z)^4} \times \left[ \pi \int \frac{I_\nu d\nu}{h\nu} + \int \frac{L_\nu d\nu \cos\theta}{h\nu 4\pi d^2} \right] \quad (10)$$

where  $\phi$  is the angle between the foreground and background quasars such that  $d = d_\perp / \sin \phi$ , and  $\theta$  is the angle between the mirror normal and the line-of-sight. Substituting the observed values into equation (10), we obtain a value for the surface brightness of  $5.3 \times 10^{-20}$  (background) +  $2.7 \times 10^{-16} \cos \theta \sin^2 \phi$  (quasar)  $\text{ erg/s/cm}^2/\text{arcsec}^2$ . This matches the observed value for a plausible geometric factor of  $0.3 = \cos \theta \sin^2 \phi$ . Approximating the absorber as

an isothermal sphere, we can compare our more sophisticated numerical results described in §3.2 directly to this system.

We can also compare our results described in §3.2 to this absorber, modeled as an SIS. We assume the quasar radiates isotropically to compute its luminosity from the observed flux. The highest predicted Ly $\alpha$  surface brightness in our image is  $3.75 \times 10^{-17} \text{erg s}^{-1} \text{cm}^{-2} \text{arcsec}^{-2}$  — a factor of  $\sim 7 \cos \theta \sin^2 \phi$  below the analytic mirror prediction and  $\sim 2.2$  below the observed value of  $0.84 \times 10^{-16} \text{erg s}^{-1} \text{cm}^{-2} \text{arcsec}^{-2}$ . For our system, while we know  $\phi$  exactly,  $\theta$  is uncertain, and we take an average value of  $\theta = 60$  degrees for our system. Our calculation is therefore a factor of  $\sim 3$  below the expectation for the mirror under these assumptions. This is compatible with the expected losses due to geometry (e.g. Ly $\alpha$  photons leak out of the system and are therefore emitted over a solid angle larger than  $2\pi$ ). We show a comparison of the surface brightness for both the analytic and numerical predictions and the observations in Table 1. for reference.

For this high incident quasar flux, the optically thick regions of the cloud are eroded by photoionization, resulting in a decreased region of high enough column density to act as an efficient fluorescent surface. For the density profile we have adopted, the bright emission region itself becomes nearly coincident with the high column-density absorber and not offset from the absorber (as in the lower flux half-moon illuminated cases). This can be seen in Figure 18 where we show the Ly $\alpha$  image, neutral column density distribution and 1D spectrum for comparison with the observations. The most significant differences between our predictions and the observations are the large absorber size and the spatially offset high Ly $\alpha$  surface brightness. This places some tension on our simple model for this system. To obtain a large surface brightness and maintain a high neutral fraction over 10 kpc scales, a large, dense sheet rather than a centrally concentrated ball may be required.

This individual system provides an exciting glimpse into what is possible by combining detailed observations of Ly $\alpha$  fluorescence and the type of predictions that are now possible. Variations in density profile, temperature structure, and velocity structure give rise to distinct signatures, with the appropriate data allowing us to discriminate between different physical mechanisms for powering the observed Ly $\alpha$  emission. Combining such modeling with larger samples of quasar-absorber pairs (e.g., Hennawi et al. 2006a, Steidel et al. 2006), one should be able to directly constrain the ensemble physical properties of the densest regions of the IGM.

#### 5.4. Future Studies

In order to make the best use of the predictions presented here, one would like to exploit both spatial and spectral information. Currently, one can already compare our Ly $\alpha$  maps and 1D spectra to observations obtained in deep long-slit spectroscopic or narrow-band surveys with follow-up slit spectroscopy (e.g. Rauch et al. 2008, Steidel et al. 2009, in prep). Blue-sensitive integral field units (or tunable narrow band filters) on large telescopes will have the capability to make channel maps of Ly $\alpha$  emission around structures, identified in imaging or spectroscopic surveys, at a given redshift that can be directly compared to the kinds of predictions that we are making here. We show such a configuration in Figure 19, which presents a series of frequency-slices through our  $z = 3$  cosmological calculation of fluorescence around a bright quasar. As the filter is tuned past Ly $\alpha$  at the appropriate redshift, the “forest” of optically thick absorbers comes into view and then fades away.

### 6. Discussion and Conclusions

We have presented our numerical methods for accurately obtaining the fluorescent Ly $\alpha$  emission signature from cosmological smoothed particle hydrodynamic simulations using these simulations in conjunction with a Monte Carlo scheme for radiative transfer of the Ly $\alpha$  line. We apply a self-shielding correction to the cosmological particle distribution to correct for the fact that the simulation is initially run in the optically thin regime, which makes particles hotter and more highly-ionized than they would have been if radiative transfer was included during the simulation. We find that one must carefully treat the boundaries between optically thin and optically thick structures to obtain accurate recovery of the neutral fraction profile within simulated structures. Failure to do this results in a systematic underprediction of the Ly $\alpha$  surface brightness and an overprediction of the sizes of high-column density structures. We find that this is sensitive to the resolution of a given simulation, and we develop techniques that are relatively robust to changes in resolution. Because SPH is notoriously problematic at boundaries, this calculation is nontrivial. However, because many widely available codes (e.g. GADGET2; Springel (2005), GASOLINE; Wadsley et al. (2004)) make use of the SPH technique, it is useful to be able to make Ly $\alpha$  predictions from this type of cosmological calculation. We further find that the treatment of temperatures in these simulations can have a significant impact on the morphology and luminosity of fluorescent Ly $\alpha$  emission from SPH cosmological simulations. While this has obvious implications for cooling radiation (which we will present in future work), it also has substantial implications for fluorescence as we show in A3. One commonly used strategy, setting *all* gas to a constant temperature  $T \sim 10^4 - 2 \times 10^4$  K, can produce misleading results

by ascribing a large amount of Ly $\alpha$  emission to high temperature, shock heated gas, which should have very low neutral fraction.

We find that in the absence of a strong ionizing continuum source, the highest *fluorescent* surface brightnesses within our  $z = 3$  simulation box are of order  $\sim 2 \times 10^{-19} \text{ erg s}^{-1} \text{ cm}^{-2} \text{ arcsec}^{-2}$ . To detect such sources will take 1500 hr campaigns on the current generation of telescopes given a typical narrow-band setup. For practical applications, we show that the fluorescent surface brightness can be substantially enhanced by the presence of powerful ionizing sources. We show that fields with bright quasars are significantly more fruitful regions to search for fluorescent Ly $\alpha$  emission from dense optically-thick structures at present, yielding significant detections in mere hours on the current generation of telescopes. Such observations can be compared directly to the calculations we present here. We test our methods and present results for the simple case of an anisotropically illuminated singular isothermal sphere to demonstrate both our method and an application of interest, and we compare these predictions to recent observations of such a system (Adelberger et al. 2006). We find that the combination of spectral shape, surface brightness, and absorber size give important constraints on the fluorescent emission from such systems. With this machinery in place, opportunities abound for understanding Ly $\alpha$  emission in the high-redshift universe.

We thank Chuck Steidel, Alice Shapley, Michael Rauch, and Kurt Adelberger for many stimulating discussions throughout the course of this work. J.A.K. and Z.Z. were supported for portions of this work by NASA through Hubble Fellowship grants HF-01197 and HF-01181 awarded by the Space Telescope Science Institute, which is operated by the Association of Universities for Research in Astronomy, Inc., for NASA, under contract NAS 5-26555. Z. Z. gratefully acknowledges support from the Institute for Advanced Study through a John Bahcall Fellowship.

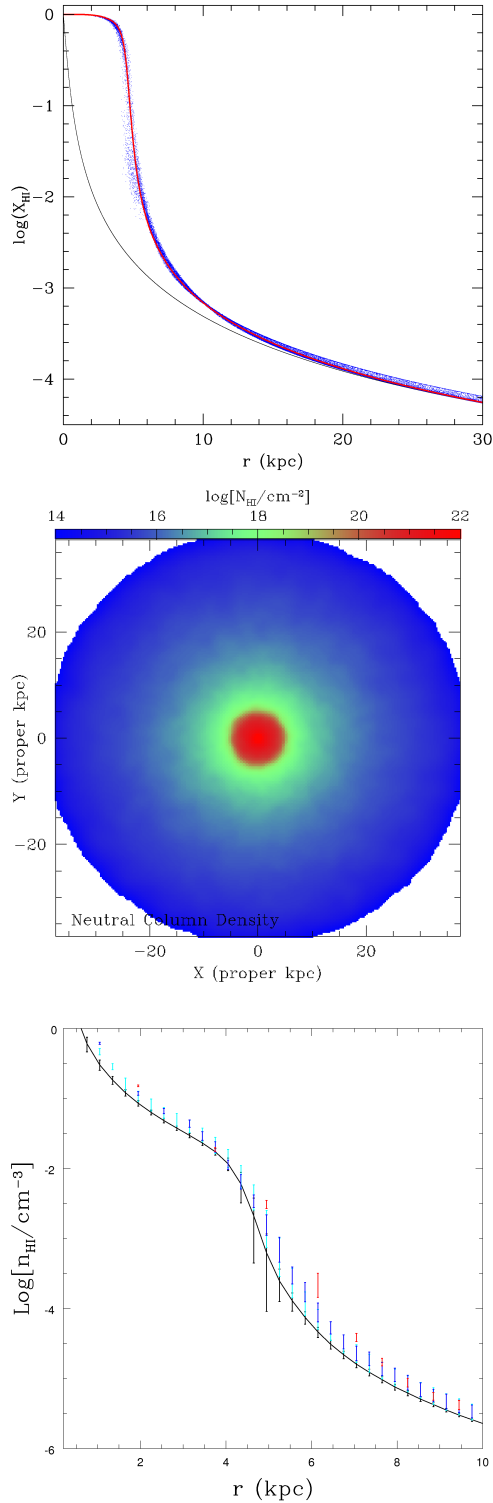


Fig. 1.— Properties for a singular isothermal sphere. Top: Neutral fraction of particles for a  $z = 3$  isothermal sphere. Black points show the optically thin case in which all particles are exposed to the same ionizing flux. Blue points show include the effect of self-shielding. The red curve shows the results of ZM02b. At the self-shielding radius ( $\sim 5$  kpc) the cloud rapidly changes from nearly transparent to nearly opaque. Middle: Projected column density distribution for the  $z = 3$  isothermal sphere. The cloud would be viewed as a DLA over a total region  $\sim 10$  kpc in diameter. Bottom: Comparison of the neutral density profile between particles and gridded cells. The black curve shows the mean and 2- $\sigma$  variation for particles as a function of radius. Red, green, and cyan correspond to the mean and 2- $\sigma$  variation for the  $32^3$ ,  $64^3$ , and  $128^3$  cells, respectively.

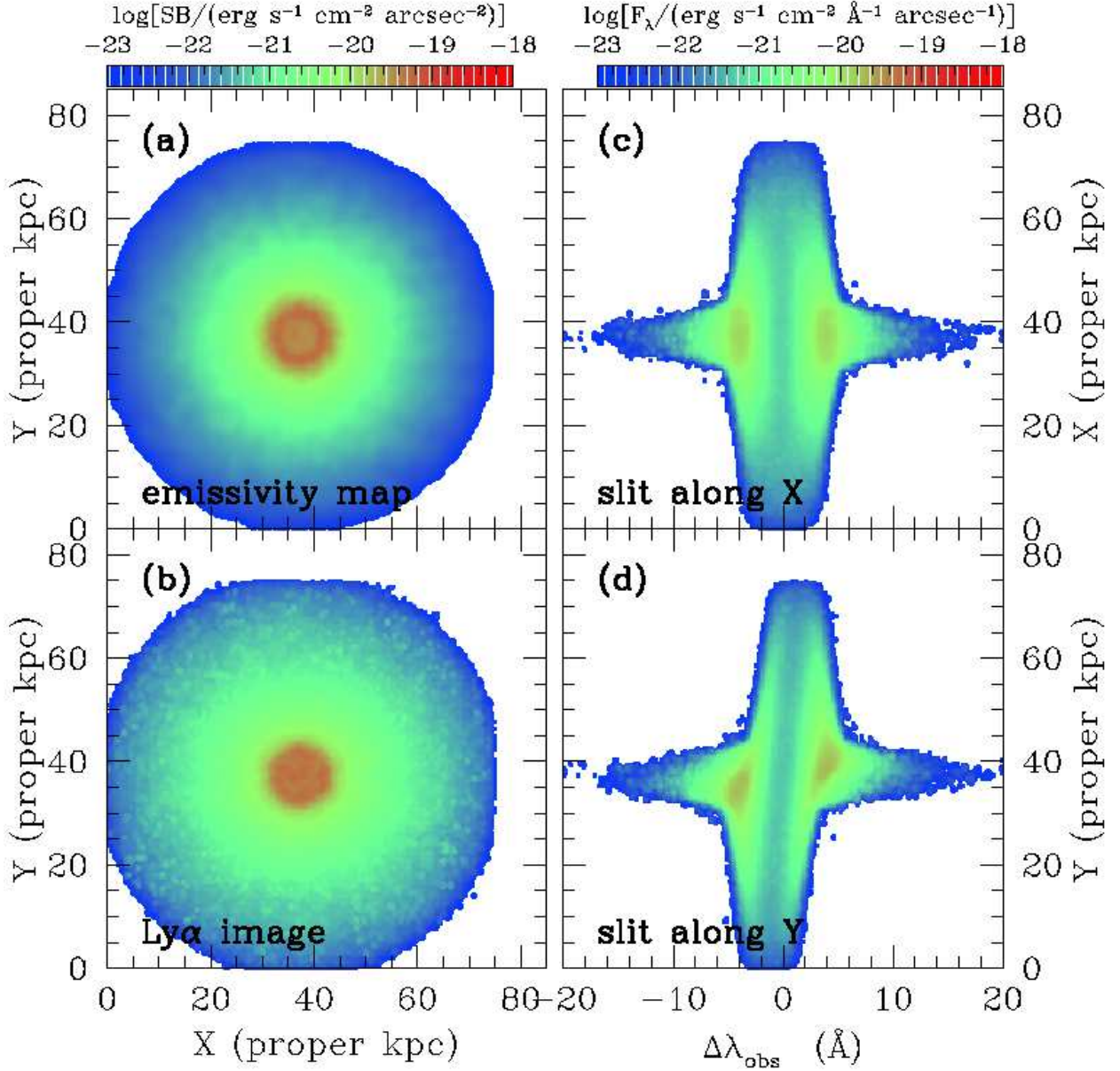


Fig. 2.— Prediction of Ly $\alpha$  emission for the  $z = 3$  isothermal sphere induced by a uniform UVB. Panels (counter-clockwise from upper left) are column emissivity, Ly $\alpha$  image, 2D spectrum when slit is placed along the y-axis, 2D spectrum when the slit is placed along the x-axis. The cloud is rotating around the x-axis in this projection. The rotation is clear in the 2D spectrum when the slit is placed along the y-axis. The Ly $\alpha$  image looks slightly smeared compared to the emissivity image. At this column density, however, the photons diffuse little in space, but rather shift in frequency to emerge from the cloud.

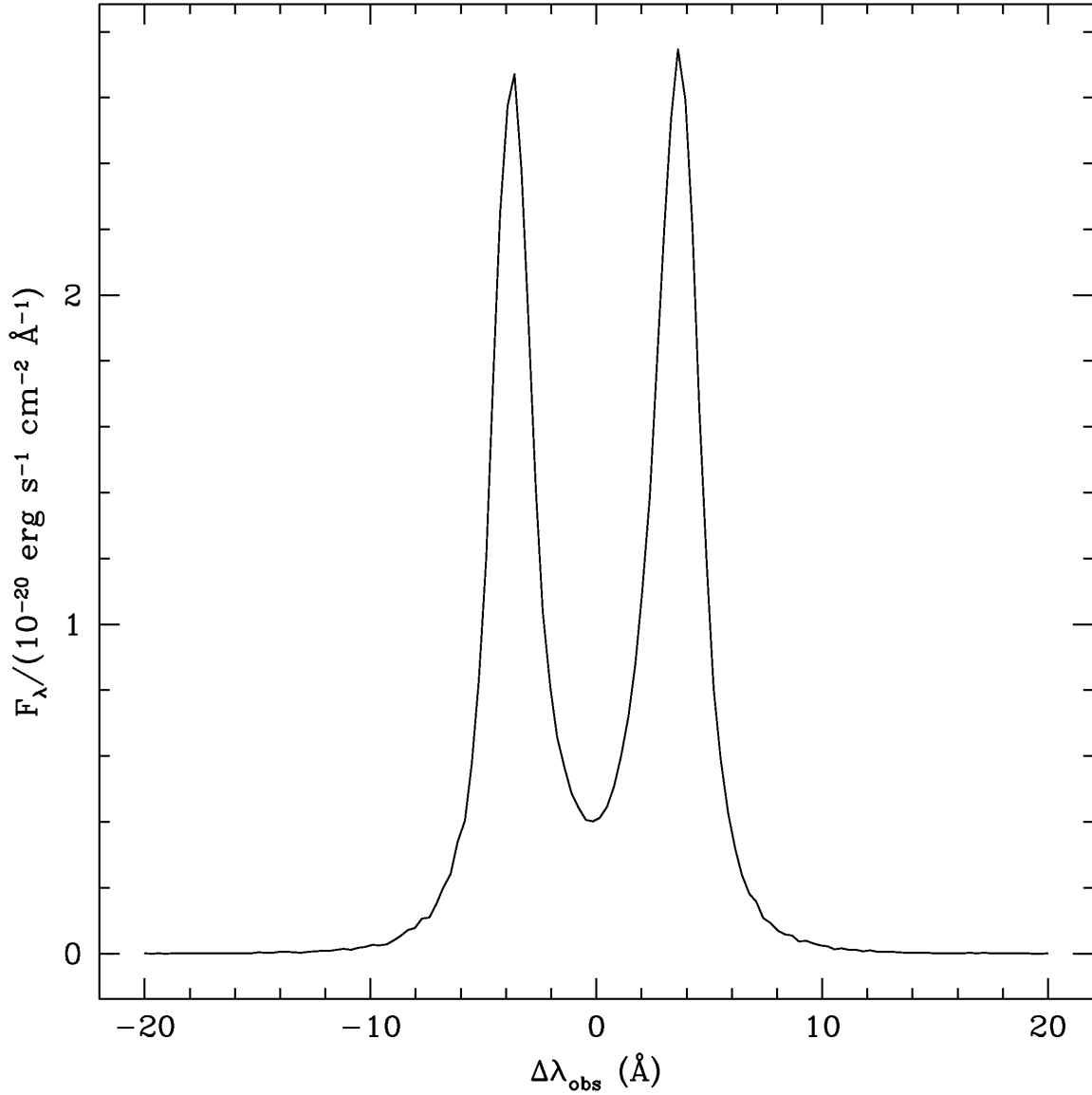


Fig. 3.— 1D spectrum of  $z = 3$  isothermal sphere induced by a uniform UVB. The spectrum is the equivalent of one that would be observed if a single fiber were placed on the sphere. The peak separation is  $\sim 7\text{\AA}$ , with positions that approximately correspond to  $\pm 4\sigma/c\lambda_{\text{Ly}\alpha}$  where  $\sigma$  is the velocity dispersion of this cloud ( $51\text{ km s}^{-1}$ ).

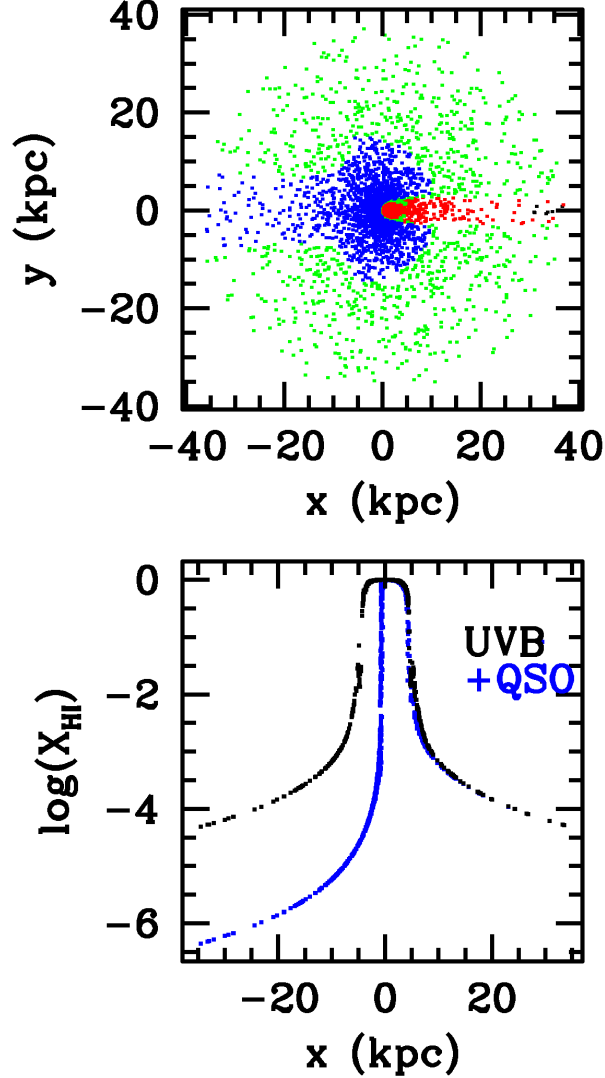


Fig. 4.— The effect of quasar flux on particle neutral fractions. Top panel: The particle distribution through a slice near the  $z = 0$  plane in the SIS color-coded according to neutral fraction *relative* to the uniform UVB case. Black, red, green, and blue points show particles for which the ratio of the neutral fraction ( $R_{HI}$ ) in the presence of the QSO to the neutral fraction in the uniform UVB case is unchanged,  $1 > R_{HI} > 0.1$ ,  $0.1 > R_{HI} > 0.01$ , and less than 0.01, respectively. Bottom Panel: The neutral Fraction of particles near the  $x$ -axis in the presence of bright QSO. The quasar is located to the left in this figure at approximately  $-500$  kpc from the center of the sphere.



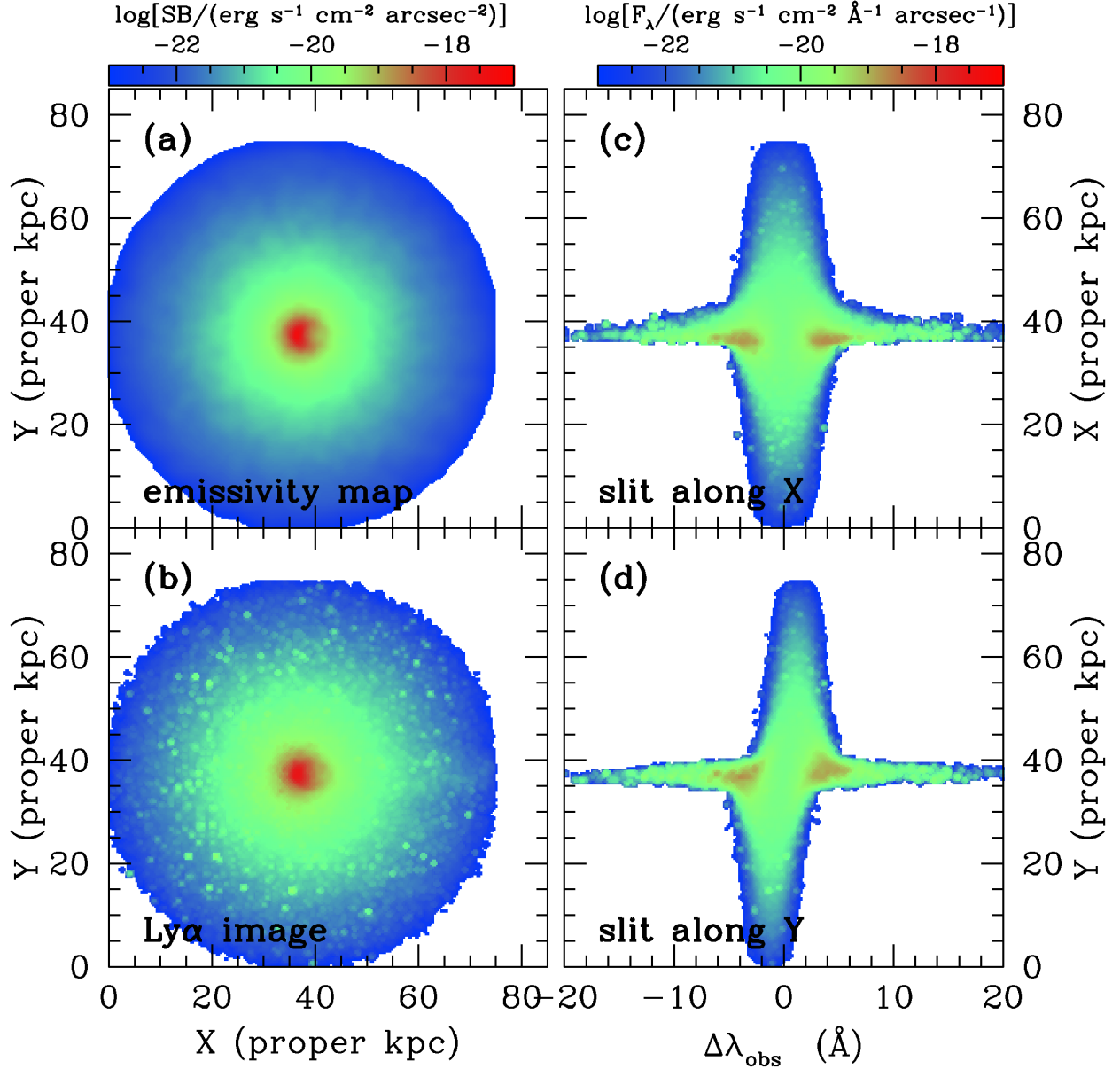


Fig. 5.— Predictions for Ly $\alpha$  emission from a  $z = 3$  isothermal sphere induced by both a uniform UVB and a bright quasar. Panels are as in Figure 2. The quasar is located to the left at a distance 500 kpc from the center of the isothermal sphere (off the panels), and has a power law continuum with slope  $-1.57$  and luminosity  $L_{\nu_L} = 1.0 \times 10^{31}$  erg s $^{-1}$ Hz $^{-1}$  at the Lyman limit. Note the difference in the color scale from Fig. 2.

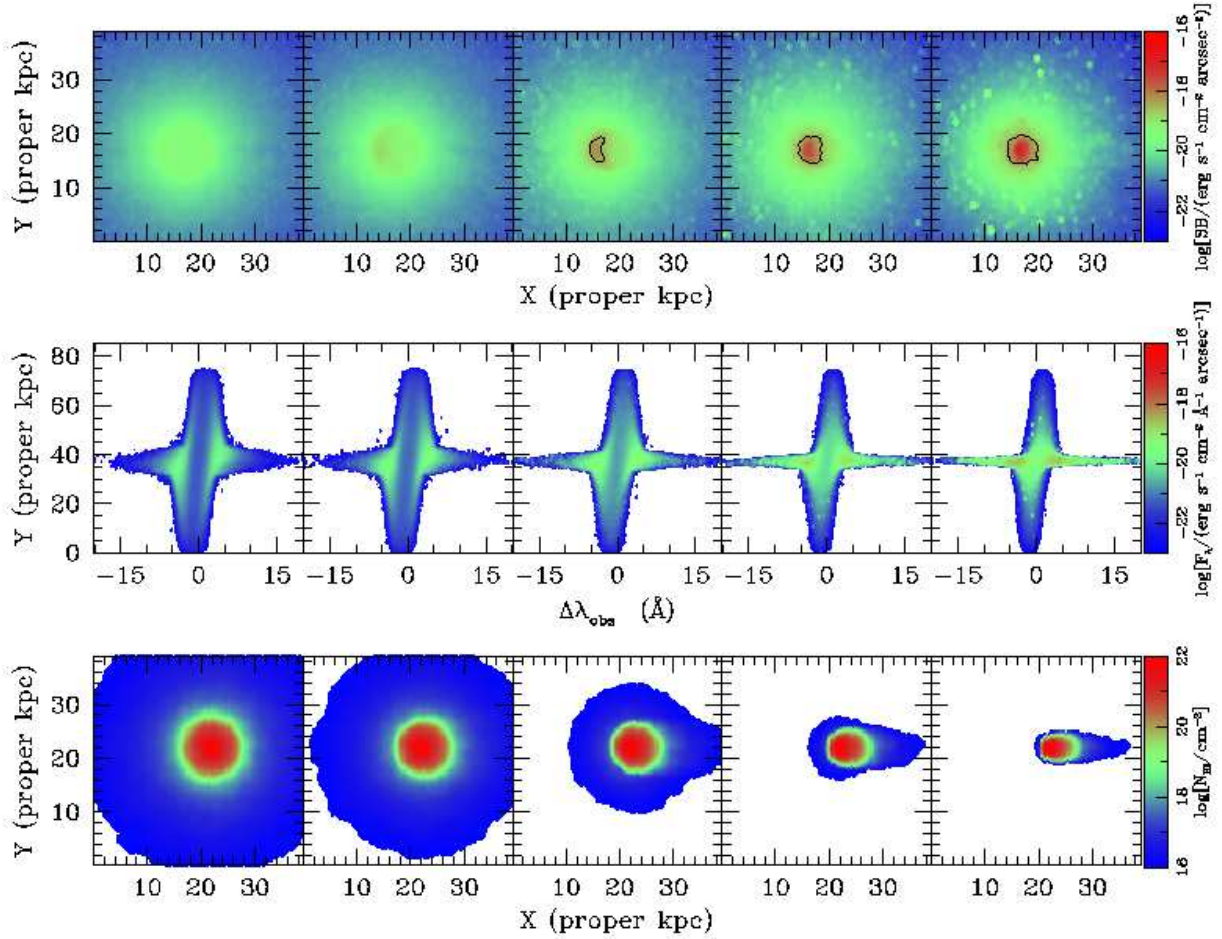


Fig. 6.— Sequences in Ly $\alpha$  surface brightness (top), 2D spectrum (middle), and neutral column density (bottom) for an isothermal sphere as a function of the illuminating quasar. The quasar is turned off in the leftmost column and the cloud is exposed to the UVB only. The quasar is located to the left at a distance 500 kpc from the center of the isothermal sphere. The quasar is turned on from specific luminosity at the Lyman limit of  $L_{\nu_L} = 1.0 \times 10^{29} \text{ erg s}^{-1} \text{ Hz}^{-1}$  to a maximum value of  $L_{\nu_L} = 1.0 \times 10^{32} \text{ erg s}^{-1} \text{ Hz}^{-1}$  in increments of factors of 10. The characteristic half moon illumination pattern is most pronounced in the middle panel, where the quasar’s radiation further ionizes the exposed area of the cloud. The black contour in the upper panel shows a constant surface brightness level of  $3 \times 10^{-19} \text{ erg s}^{-1} \text{ cm}^{-2} \text{ arcsec}^{-2}$ . The bright emission comes from gas that would have high neutral density in the absence of the quasar flux, and has a high recombination rate once the quasar radiation impinges upon it. This demonstrates the increasing tendency of the quasar to fully ionize the outer edges of the cloud, and to shrink the highly neutral regions of the cloud from the left.

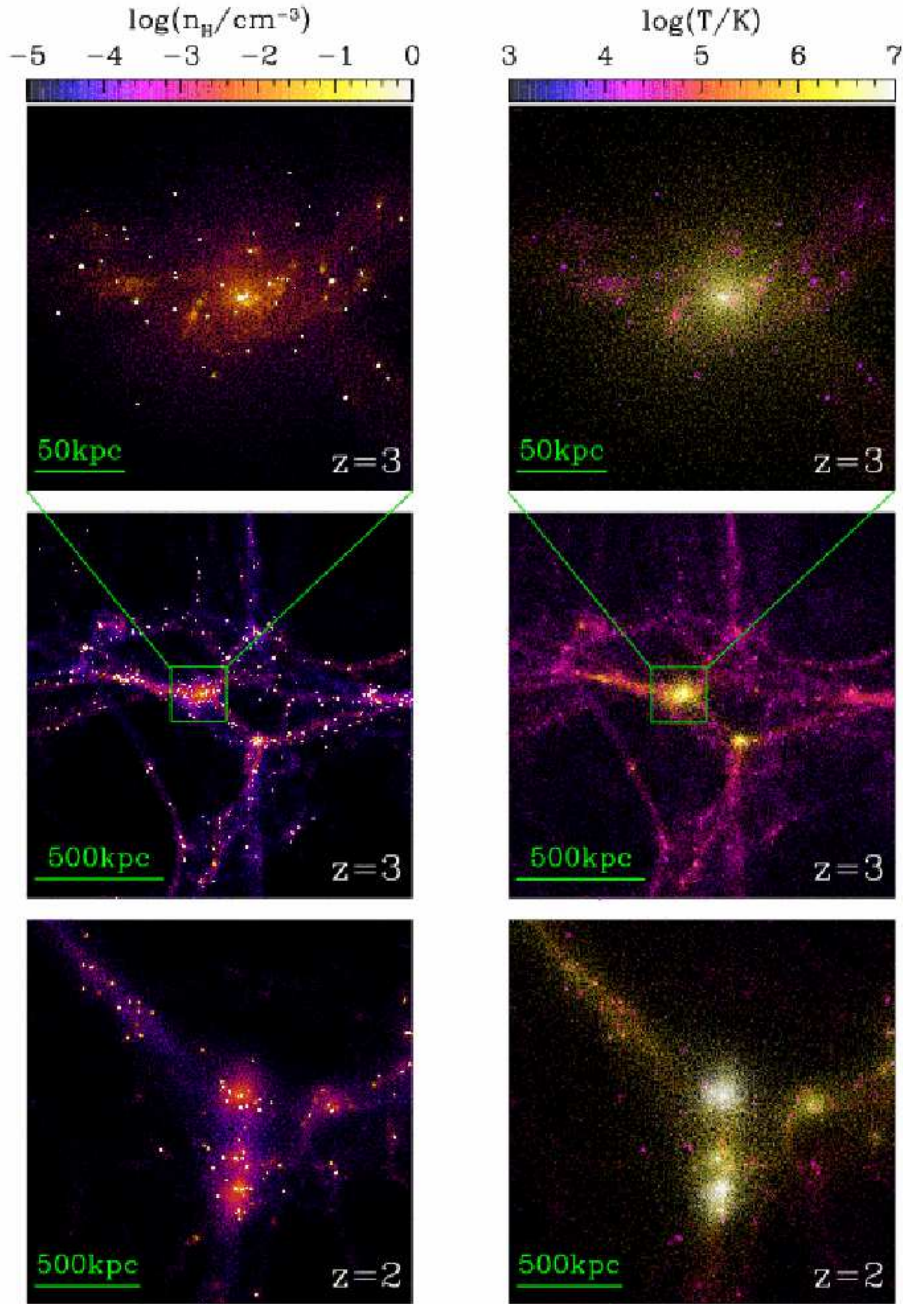


Fig. 7.— Physical properties of the cosmological volumes analyzed. Gas density is shown on the left and gas temperature on the right. The middle panels are for the 1.5 Mpc (physical) sub-region of the  $5.555 h^{-1}$  Mpc (comoving) simulation box at  $z = 3$ . Upper panels show a 200 kpc region extracted from within the region shown in the middle panels. Bottom panels show a 1.8 Mpc (physical) sub-region extracted from the  $22.222 h^{-1}$  Mpc (comoving) simulation box.

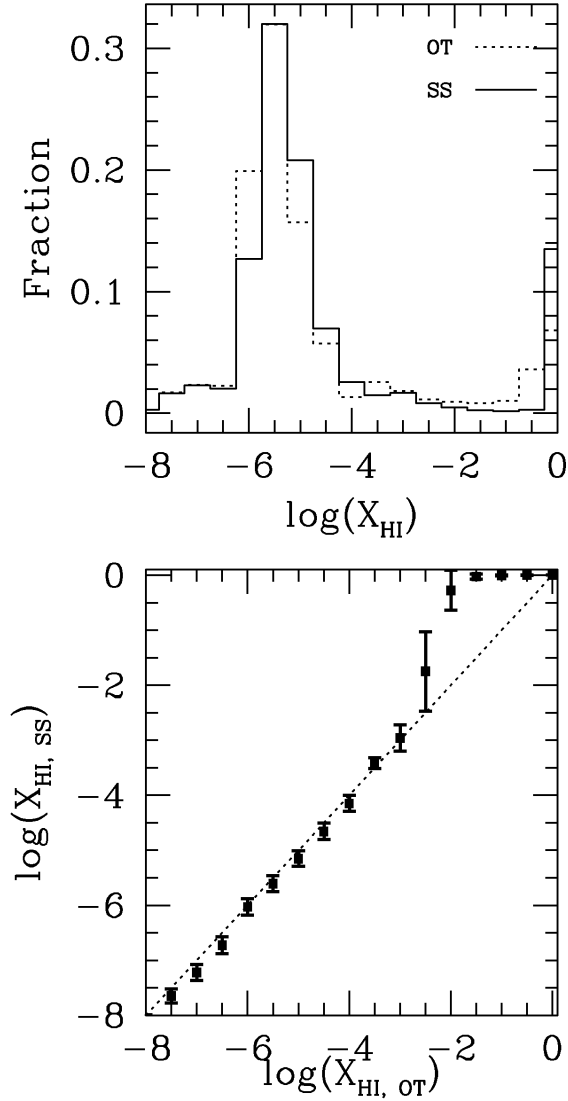


Fig. 8.— The upper panel shows the distribution of neutral fraction ( $X_{\text{HI}}$ ) for self-shielded particles compared to the optically thin approximation in the L5 simulation. The bottom panel shows the optically-thin (OT) versus self-shielded (SS) neutral fraction particle-by-particle. The effect of self-shielding is to move dense particles to higher neutral fractions, which is particularly important at large values of the neutral fraction.

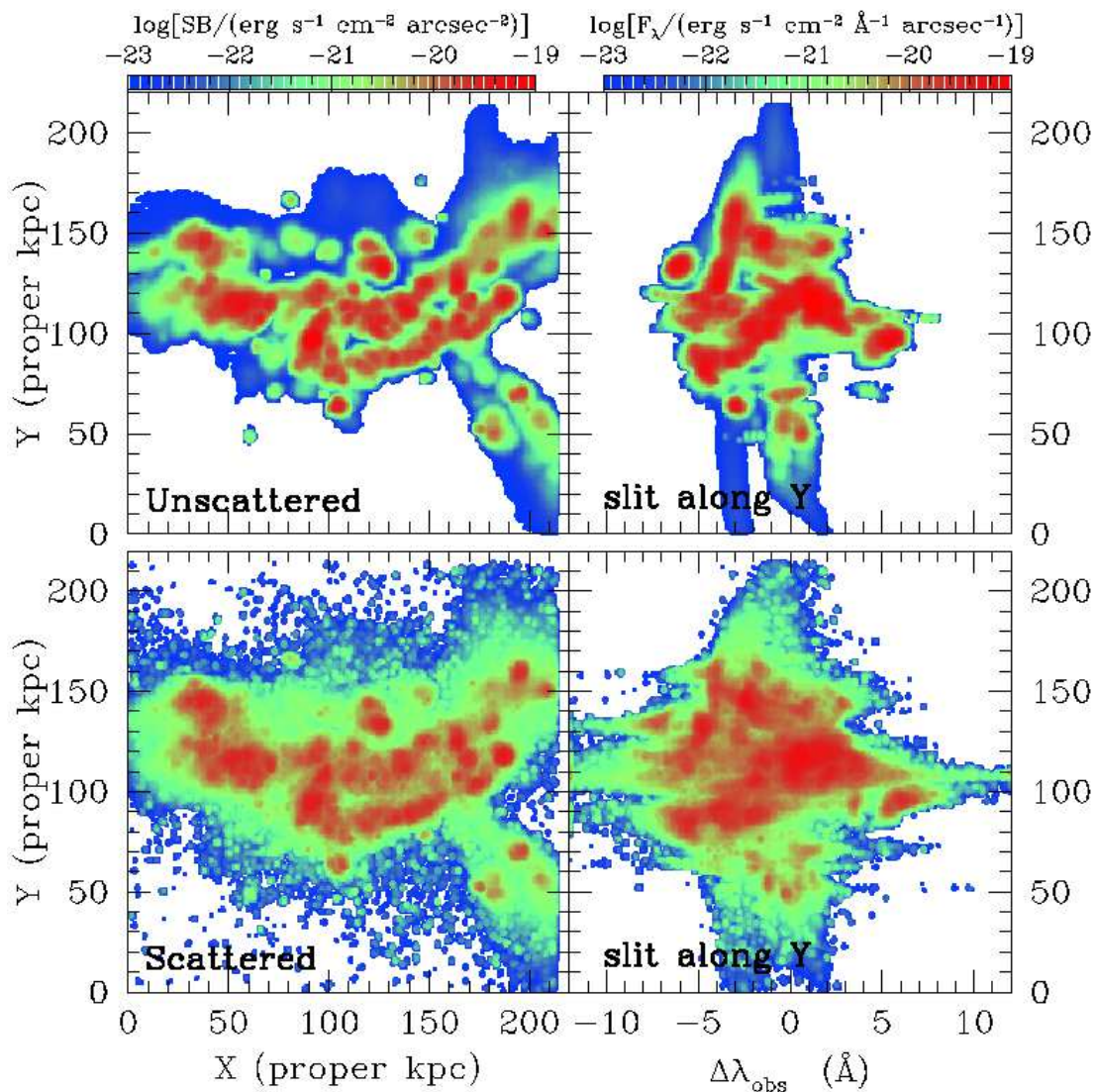


Fig. 9.— Ly $\alpha$  map of the central region of the L5 simulation. This projection corresponds to the upper panels in Fig. 7. Left panels show Ly $\alpha$  surface brightness and right panels show the 2D spectrum with slit along the  $y$ -direction. The upper panels show the image and spectrum one obtains without radiative transfer. Bottom panels show the post-radiative transfer image and spectrum.

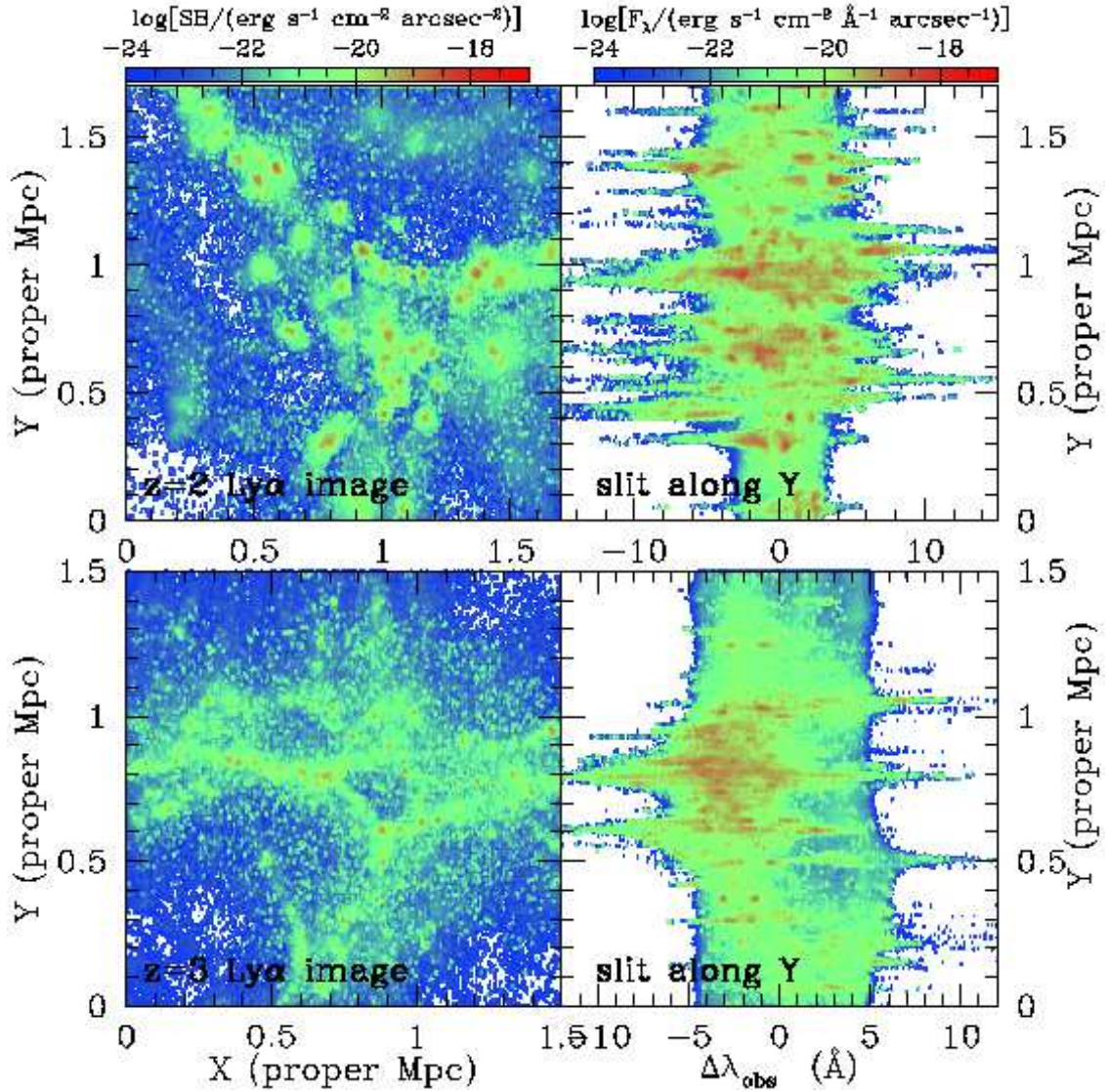


Fig. 10.— Ly $\alpha$  fluorescence from cosmological simulations. Top: Emission at  $z = 2$  from the gas distribution in a sub-region of size 1.8 Mpc from cosmological simulation L22. Left panel shows the Ly $\alpha$  surface brightness and right panel shows the 2D spectrum with slit along the  $y$ -direction. Bottom: Emission at  $z = 3$  from a sub-region of size 1.5 Mpc from cosmological simulation L5. Note the surface brightness scale is different from Figure 9.

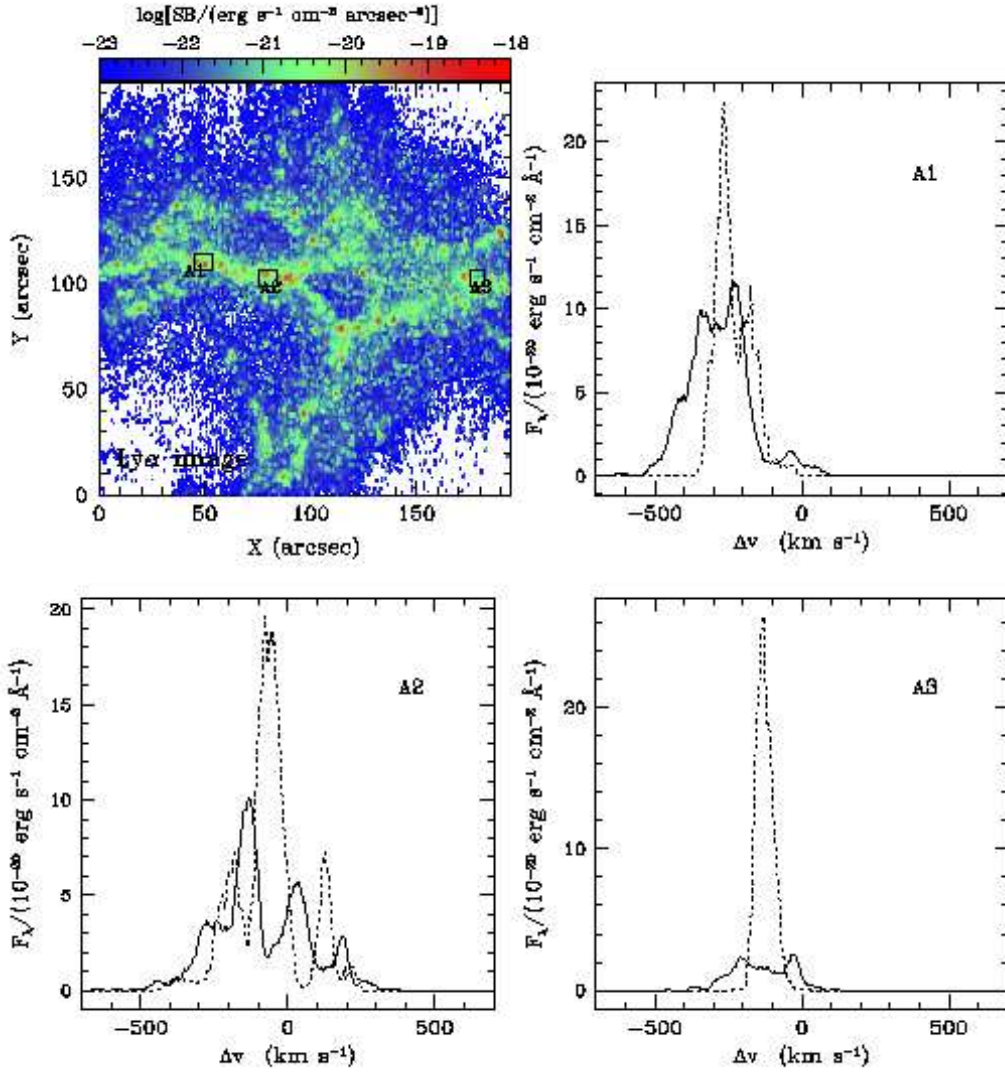


Fig. 11.— 1D spectra from multiple apertures throughout the  $z = 3$  structure in Figure 10. The top-left panel shows the Ly $\alpha$  image (as in Figure 10) with 3 square apertures ( $7.5'' \times 7.5''$ ) overlaid. The other three panels show the 1D spectra from the three apertures, respectively. Solid lines in the figure show the post-transfer spectra and dotted lines show the case in which the photons are not scattered.

Table 1. Comparison of observed surface brightness for the system seen in Adelberger et al. (2006) with two theoretical models for the system.

System	Surface Brightness ( $\text{erg s}^{-1}\text{cm}^{-2} \text{arcsec}^{-2}$ )
Observed Value	$0.84 \times 10^{-16}$
Analytic Mirror Prediction	$2.7 \times 10^{-16} \cos \theta \sin^2 \phi$
SIS + Radiative Transfer	$0.4 \times 10^{-16}$



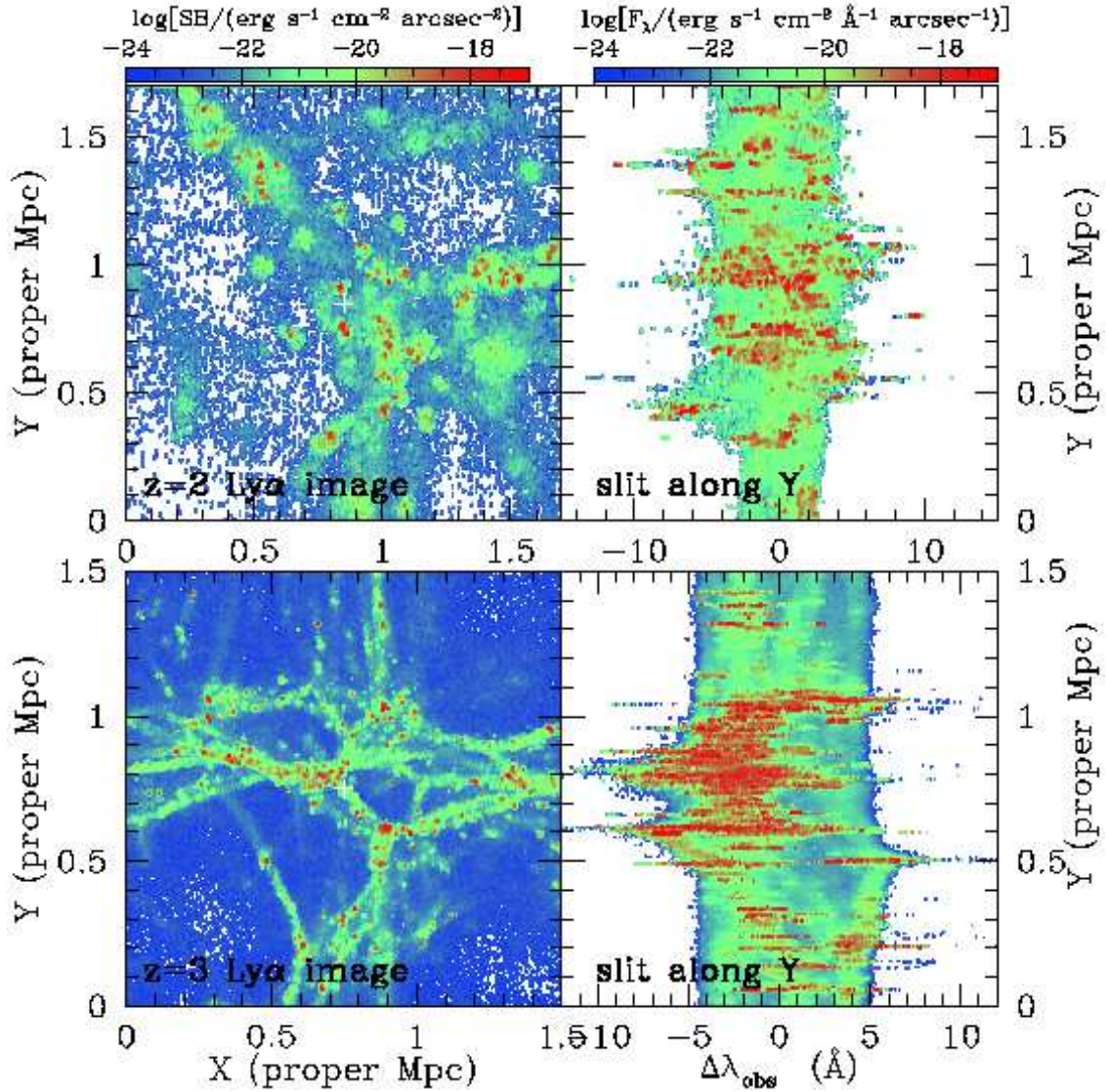


Fig. 12.— Ly $\alpha$  maps including a quasar source. Panels are as in Fig. 10 but we have now placed a bright quasar with Lyman limit luminosity  $L_{\nu_L} = 1.0 \times 10^{32} \text{ erg s}^{-1} \text{ Hz}^{-1}$  at the center of the region (marked with crosses). Left panels show the Ly $\alpha$  surface brightness on the sky for redshifts  $z = 2$  (upper panels) and  $z = 3$  (lower panels). Right panels show the 2D spectrum with slit along the  $y$ -direction from the images shown in the left.

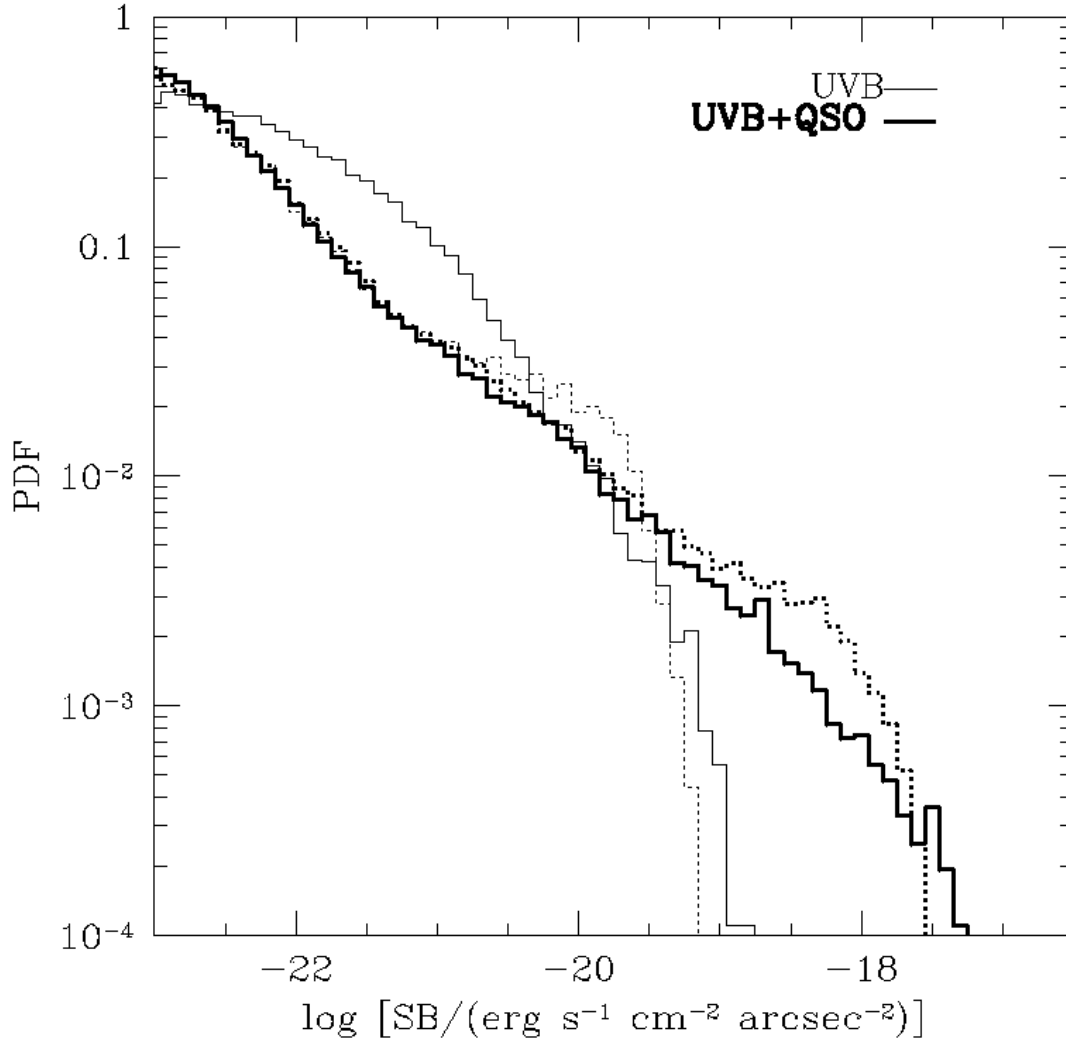


Fig. 13.— Distributions of resultant Ly $\alpha$  surface brightness of pixels for the UVB case and the UVB+QSO case. Solid (dotted) thin lines show the UVB-only case and solid (dotted) thick lines show the UVB+QSO pixel distribution after (before) Ly $\alpha$  radiative transfer. The shift toward higher surface brightness pixels results directly from the quasar radiation impinging on the dense, optically thick clouds in the simulation.

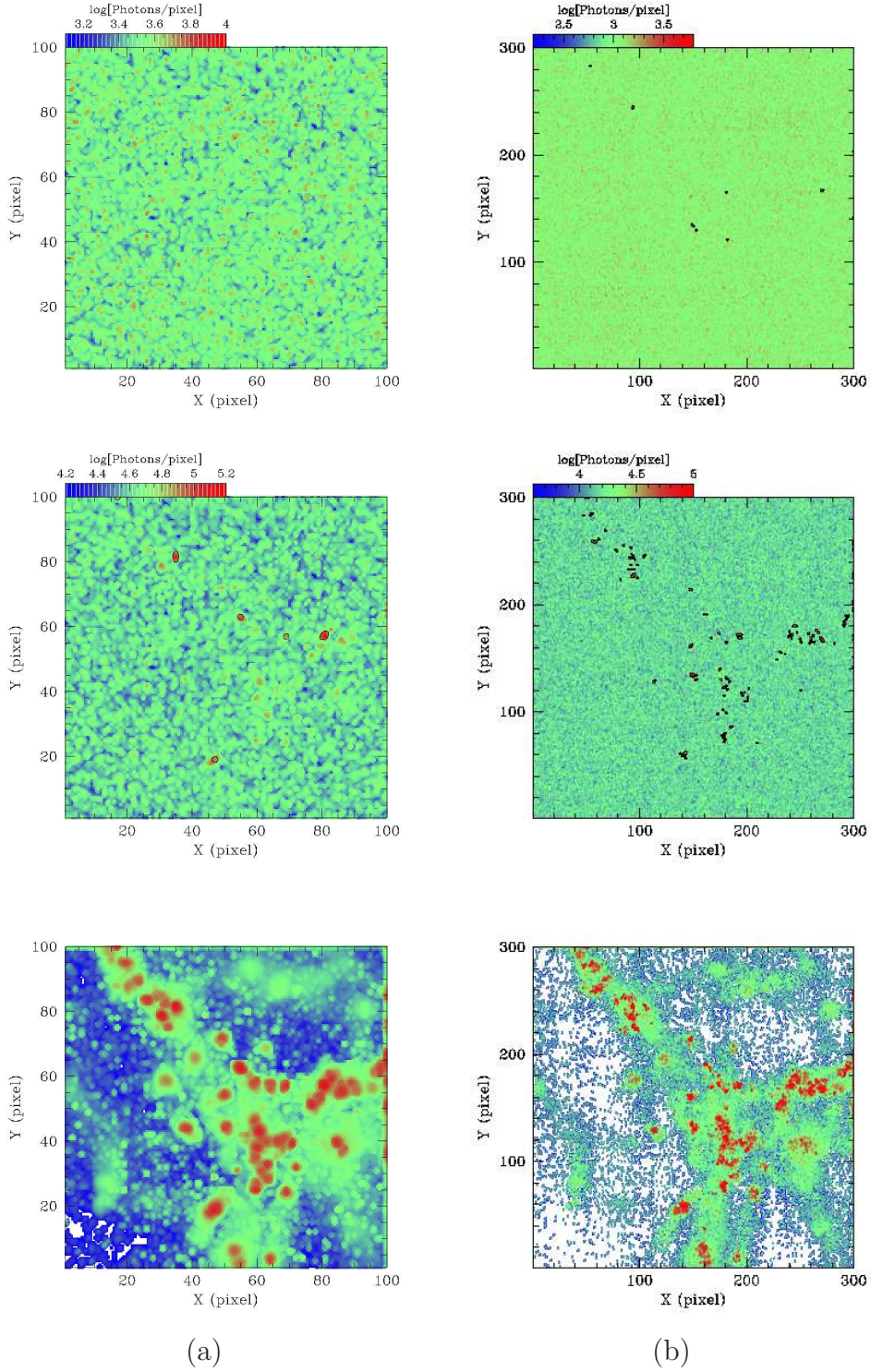


Fig. 14.— Simulated observed maps of Ly $\alpha$  fluorescence in the L22 region at  $z = 2$ . Top panels show a 10 hour observation using a 10  $\text{\AA}$  filter on a 10m telescope with 30% efficiency. Middle panels show a 1500 hour integration. Bottom panels show the noiseless image to aid with identifying features in the noisy maps. Left panels are the case for fluorescence from the UVB only. Right panels are for fluorescence boosted by the presence of a bright quasar with  $L_{\nu_L} = 1.0 \times 10^{32} \text{ erg s}^{-1} \text{ Hz}^{-1}$  at the center of the region. The pixels in these images are roughly 2x2 and 1x1 arcsec<sup>2</sup> for the left and right panels respectively. Ellipses in the maps show sources identified by SExtractor.

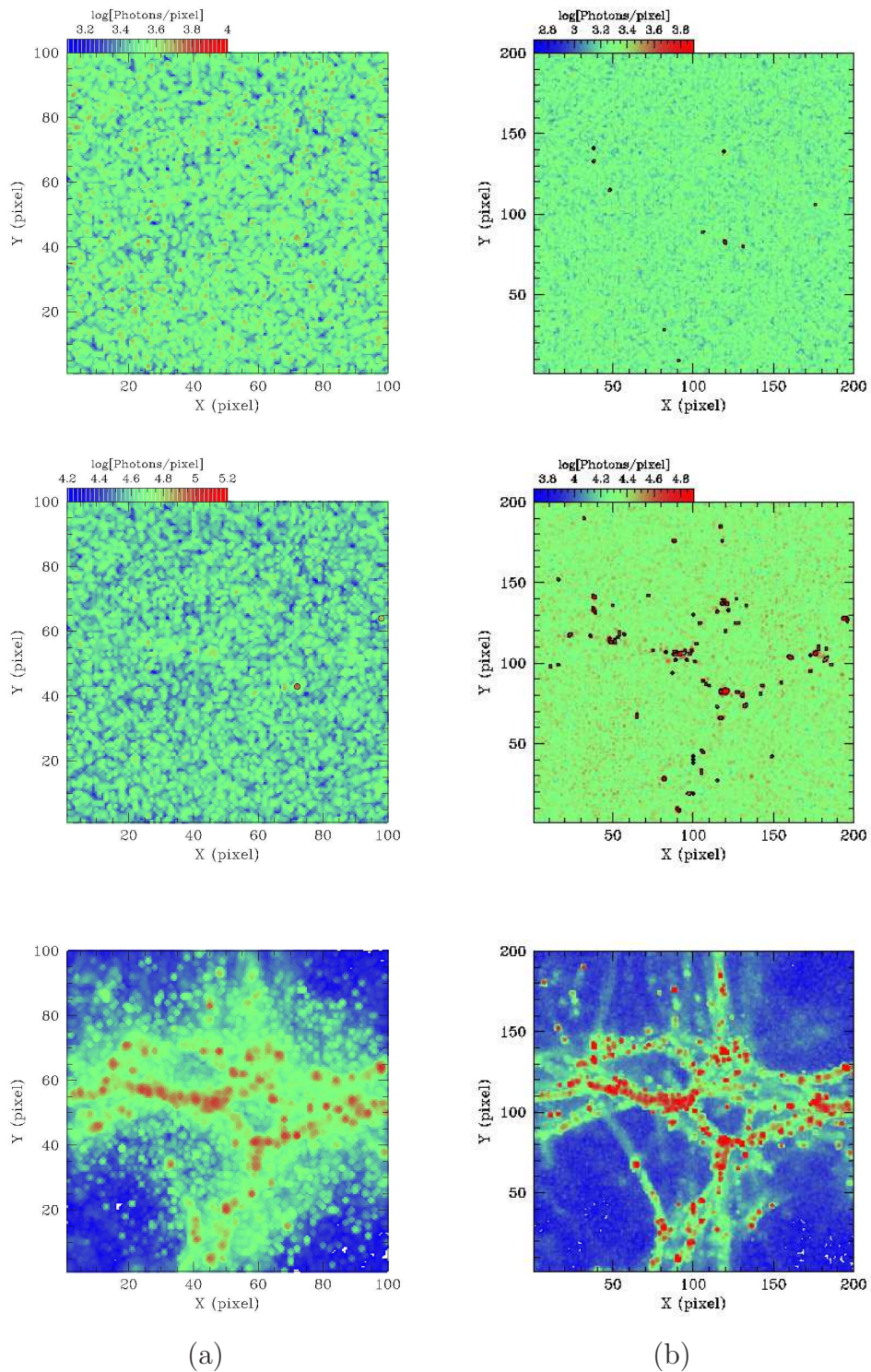


Fig. 15.— Simulated observed maps of Ly $\alpha$  fluorescence in the L5 region at  $z = 3$ . Top panels show a 10 hour observation using a 10 $\text{\AA}$  filter on a 10m telescope with 30% efficiency. Middle panels show a 1500 hour integration. Bottom panels show the noiseless image to aid with identifying features in the noisy maps. Left panels are the case for fluorescence from the UVB only. Right panels are for fluorescence boosted by the presence of a bright quasar.

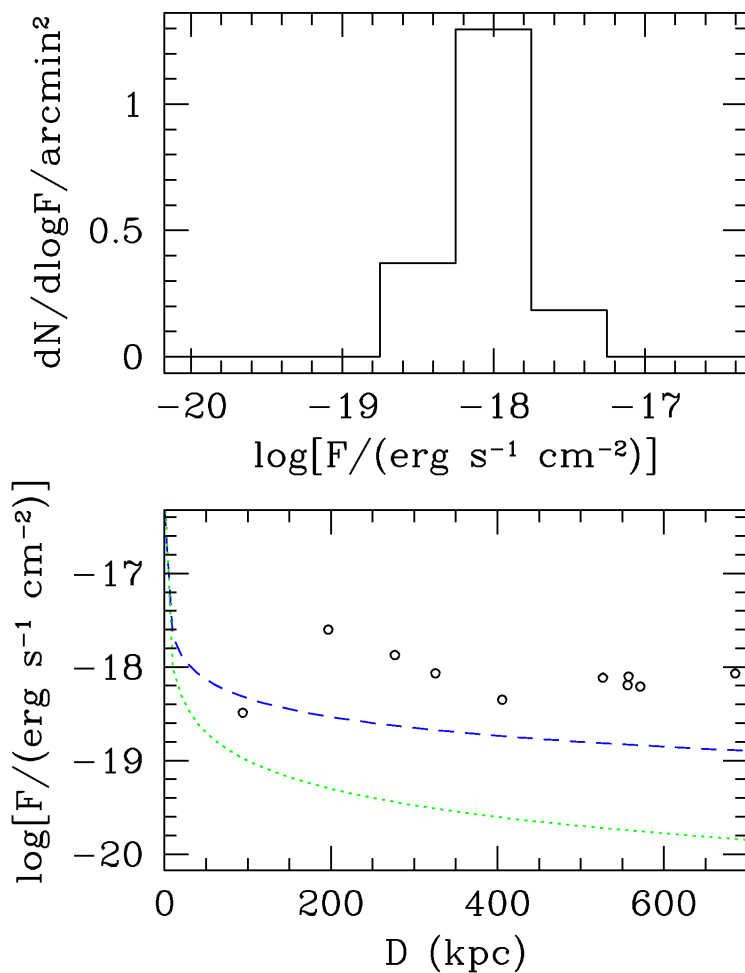


Fig. 16.— Distribution of Ly $\alpha$  sources for the UVB+QSO case identified from simulated noisy images for a 10 hr exposure using the Source Extractor software. The top panel shows the differential distribution in flux of identified sources. The bottom panel shows the source fluxes as a function of projected distance from the center of the image, where the QSO is located. The dashed curve in the lower panel shows a  $d^{-2/3}$  decay, which would be expected for a population of identical, self-shielded isothermal spheres. The dotted curve shows a  $d^{-2}$  decay.

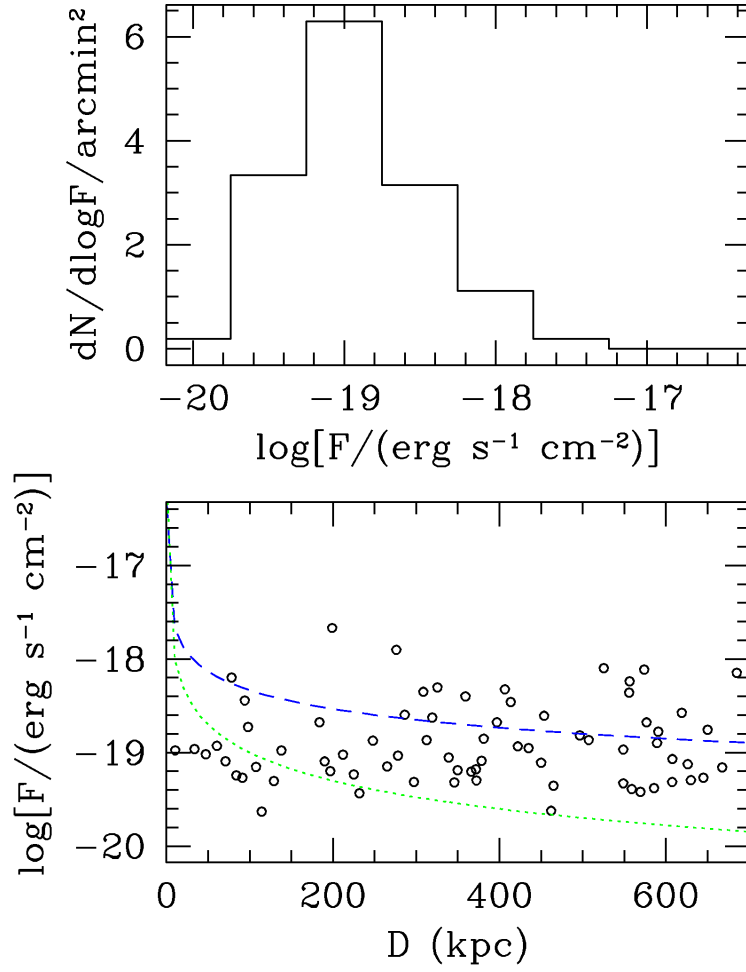


Fig. 17.— The same as Fig. 16 for a 1500 hour exposure. Again we detect a radial trend but not an inverse-square dependence.

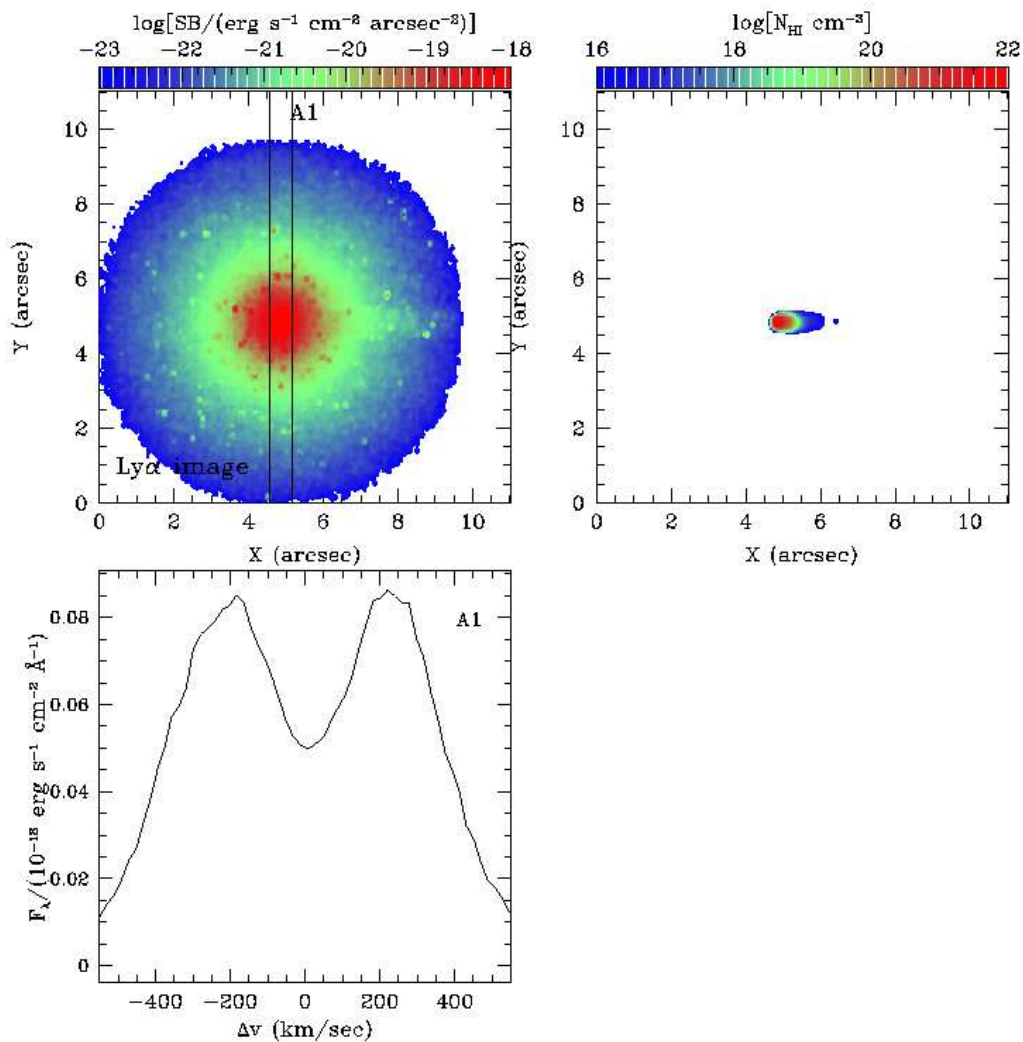


Fig. 18.— A detailed model of the system observed by Adelberger et al. (2005). The cloud is modeled as a singular isothermal sphere anisotropically illuminated by a quasar from the left. The upper left panel shows the Ly $\alpha$  image for this configuration. Vertical lines in this panel show a long-slit with 0.7 arcsec slit width placed along the edge of the cloud. We plot the 1-d spectrum from this aperture in the lower left panel. The upper right panel shows the neutral column density distribution from the cloud.

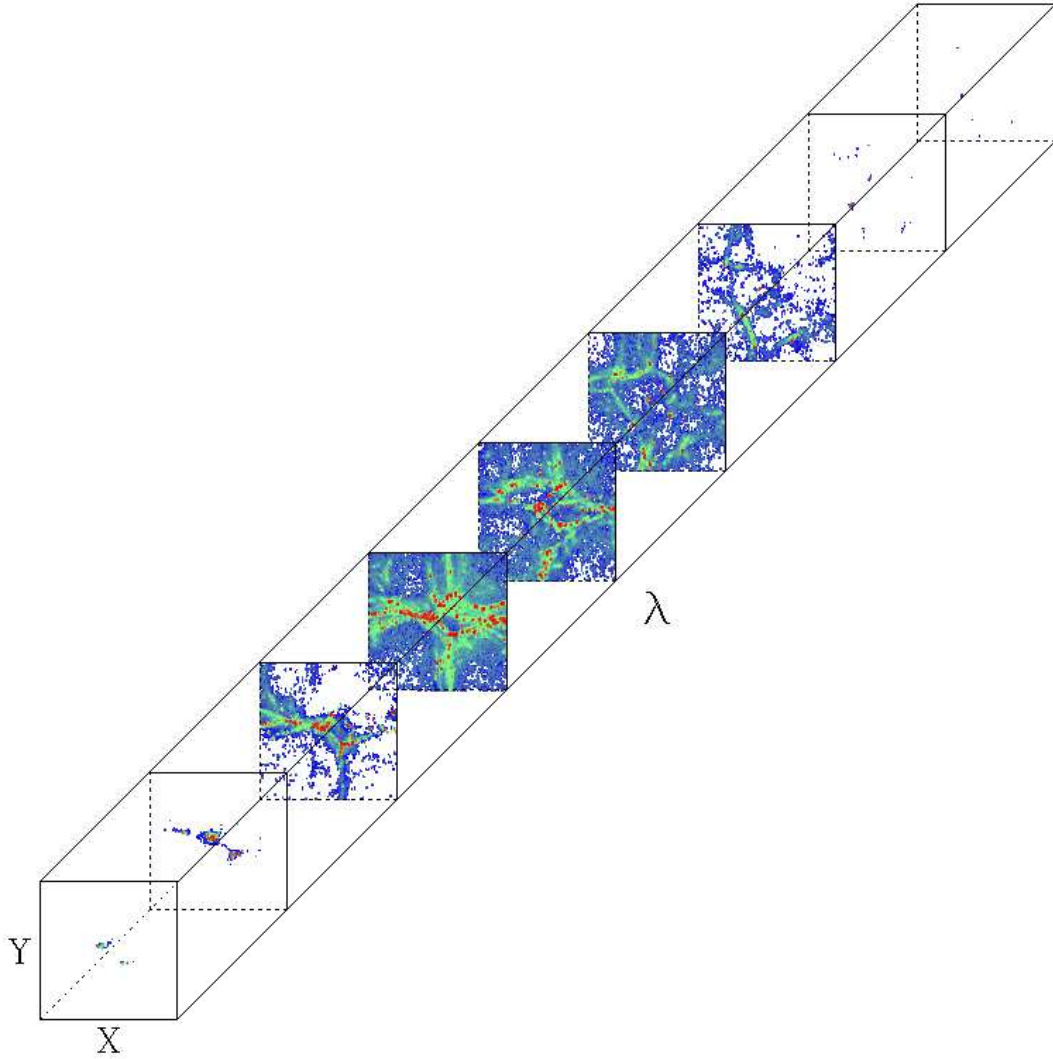


Fig. 19.— Channel maps of Ly $\alpha$  fluorescence around a bright quasar. The channels are 0.33 Å in width and spaced by 0.66 Å. An IFU on a large telescope could in principle produce data for direct comparison with maps such as these constructed from the simulations.



## REFERENCES

- Adelberger, K. L., Steidel, C. C., Kollmeier, J. A., & Reddy, N. A. 2006, *ApJ*, 637, 74
- Bahcall, J. N., & Salpeter, E. E. 1965, *ApJ*, 142, 1677
- Bahcall, J. N., & Salpeter, E. E. 1966, *ApJ*, 144, 847
- Bahcall, J. N., Peterson, B. A., & Schmidt, M. 1966, *ApJ*, 145, 369
- Barnes, J., & Hut, P. 1986, *Nature*, 324, 446
- Bertin, E., & Arnouts, S. 1996, *A&AS*, 117, 393
- Binney, J. 1977, *ApJ*, 215, 483
- Cantalupo, S., Porciani, C., Lilly, S. J., & Miniati, F. 2005, *ApJ*, 628, 61
- Cantalupo, S., Lilly, S. J., & Porciani, C. 2007, *ApJ*, 657, 135
- Croft, R. A. C., Weinberg, D. H., Katz, N., & Hernquist, L. 1998, *ApJ*, 495, 44
- Dave, R., Dubinski, J., & Hernquist, L. 1997, *New Astronomy*, 2, 277
- Dey, A., et al. 2005, *ApJ*, 629, 654
- Dijkstra, M., Haiman, Z., & Spaans, M. 2006, *ApJ*, 649, 37
- Dijkstra, M., Haiman, Z., & Spaans, M. 2006, *ApJ*, 649, 14
- Fardal, M. A., Katz, N., Gardner, J. P., Hernquist, L., Weinberg, D. H. & Davé, R. 2001, *ApJ*, 562, 605
- Francis, P. J., & Bland-Hawthorn, J. 2004, *MNRAS*, 353, 301
- Furlanetto, S. R., Schaye, J., Springel, V., & Hernquist, L. 2005, *ApJ*, 622, 7
- Gingold, R. A., & Monaghan, J. J. 1977, *MNRAS*, 181, 375
- Gould, A., & Weinberg, D.H., 1996, *ApJ*, 468, 462
- Haardt, F. & Madau, P. 1996, *ApJ*, 461, 20
- Haiman, Z., Spaans, M., & Quataert, E. 2000, *ApJ*, 537, L5
- Hansen, M., & Oh, S. P. 2006, *MNRAS*, 367, 979

- Hennawi, J. F., et al. 2006, *ApJ*, 651, 61
- Hennawi, J.F., Procahnska, J.X., Kollmeier, J.A., & Zheng, Z. *ApJ*, 693, L49
- Hernquist, L. 1987, *ApJS*, 64, 715
- Hernquist, L., & Katz, N. 1989, *ApJS*, 70, 419
- Hernquist, L., Katz, N., Weinberg D.H. & Miralda-Escudé 1996 *ApJ*, 457, L51
- Hogan, C.J., & Weymann, R.J., 1987, *MNRAS*, 225, P1
- Hui, L., & Gnedin, N. Y. 1997, *MNRAS*, 292, 27
- Katz, N. 1992, *ApJ*, 391, 502
- Katz, N., Weinberg D.H. & Hernquist, L. 1996, *ApJS*, 105, 19 (KWH)
- Katz, N., Hernquist, L., & Weinberg, D. H. 1999, *ApJ*, 523, 463
- Kereš, D., Katz, N., Weinberg, D. H., & Davé, R. 2005, *MNRAS*, 363, 2
- Kirkman, D., Tytler, D., Suzuki, N., Melis, C., Hollywood, S., Kory, J., So, G., Lubin, D., Jena, T., Norman, M.L., & Paschos, P., 2005, *MNRAS*, 360, 1373
- Liske, J., & Williger, G. M. 2001, *MNRAS*, 328, 653
- Lucy, L. B. 1977, *AJ*, 82, 1013
- Lynds, R. 1971, *ApJ*, 164, L73
- Matsuda, Y., Yamada, T., Hayashino, T., Yamauchi, R., & Nakamura, Y. 2006, *ApJ*, 640, L123
- Miralda-Escudé, J., Cen, R., Ostriker, J. P., & Rauch, M. 1996, *ApJ*, 471, 582
- Monaghan, J. J., & Lattanzio, J. C. 1985, *A&A*, 149, 135
- Osterbrock, D.E., 1962 *ApJ*, 135, 95
- Ouchi, M., Shimasaku, K., Akiyama, M. , et al. 2005, *ApJ*, 620, L1
- Padmanabhan, T., 1993 *Structure Formation in the Universe* (Cambridge: Cambridge Univ. Press)

- Rauch, M., Haehnelt, M., Bunker M., Becker, G., Marleau, F., Graham, J., et al., 2008, ApJ, 681, 856
- Spitzer, L., 1978, Physical Processes in the Interstellar Medium (New York: Wiley)
- Springel, V. 2005, MNRAS, 364, 1105
- Steidel, C.C., Adelberger, K.L, Shapley, A., Pettini, M., Dickinson, M., & Giavalisco, M. . 2000, ApJ, 532, 170
- Tasitsiomi, A. 2006, ApJ648, 762
- Telfer, R. C., Zheng, W., Kriss, G. A., & Davidsen, A. F. 2002, ApJ, 565, 773
- Wadsley, J. W., Stadel, J., & Quinn, T. 2004, New Astronomy, 9, 137
- Zhang, Y., Anninos, P., & Norman, M. L. 1995, ApJ, 453, L57
- Zheng, Z. & Miralda-Escudé, J.M., 2002a ApJ, 578, 33 (ZM02)
- Zheng, Z. & Miralda-Escudé, J.M., 2002b ApJ, 568, L71 (ZM02b)

### A. Accurate Self-shielding Correction

In the SPH technique, the smooth density field is represented by discrete particles. One must therefore always be cautious that there are sufficient particles to adequately resolve structures of interest. In this application, we are primarily concerned with resolving the optically thick skins of dense gas clouds within our simulation volume. While the clouds themselves are well-resolved, usually with several hundred to thousands of particles (in our L5 simulation), it is the distribution of particles at the interface between optically thick and optically thin regions that contribute the majority of the Ly $\alpha$  emission. We, therefore, must pay close attention to the accuracy of our self-shielding correction at these transition layers. We develop a method to perform the self-shielding correction that accounts for the effects of low resolution, and we test this method using a series of SPH approximations to an isothermal sphere (for which we have exact analytic results).

To perform the self-shielding correction for a given particle distribution we determine the optical depth for photons to reach each particle’s position. We do this by evaluating

the attenuated ionizing photon intensity along 6 directions (and the quasar direction when present). In the SPH technique, each particle has a density distribution defined by its mass and smoothing length. At a given particle’s position, the optical depth for ionizing photons towards a direction can be straightforwardly computed by integrating the neutral density profiles of those particles that contribute in this direction. However, because of the finite size of particles and the steep gradient in the neutral density profile near the self-shielding layer, such a simple computation may lead to large errors in the optical depth and thus an inaccurate self-shielding correction. The problem is analogous to computing the optical depth from a steep density distribution by using finite rectangle bins and evaluating the density at the center of each bin. To compute the optical depth to the center of a bin, the contribution from that bin is evaluated as the density at the bin center times the half-width of the bin. If the gradient of the density profile is large, this obviously overestimates the contribution to the optical depth in the direction of decreasing density. A better way of computing the contribution is to use the trapezoidal rule in this bin with the shape of the trapezoid determined by the gradient of the density distribution. We apply a similar idea for computing the optical depth from the SPH particle distribution.

In the SPH formalism, the density at a given position  $\mathbf{r}_0$  is given by:

$$\rho(\mathbf{r}_0) = \sum_i^N m_i W(\mathbf{r}_0; \mathbf{r}_i, h_i) = \sum_{i=0}^N \frac{m_i}{(\sqrt{2\pi}h_i)^3} \exp\left(-\frac{|\mathbf{r}_0 - \mathbf{r}_i|^2}{2h_i^2}\right) \quad (\text{A1})$$

where  $W(\mathbf{r}_0; \mathbf{r}_i, h_i)$  is the 3D Gaussian equivalent of the SPH cubic spline kernel used in the simulation<sup>11</sup>,  $N$  is the number of particles that contribute to the density at  $\mathbf{r}_0$  having position, neutral mass, smoothing length  $\mathbf{r}_i, m_i, h_i$ . For each particle we evaluate the density gradient at the position of the particle,  $\mathbf{r}_0$  as

$$\nabla\rho|_0 = \sum_{i=0}^N m_i \nabla W(\mathbf{r}_0; \mathbf{r}_i, h_i) = - \sum_{i=0}^N \frac{\mathbf{r}_0 - \mathbf{r}_i}{h_i^2} \frac{m_i}{(\sqrt{2\pi}h_i)^3} \exp\left(-\frac{|\mathbf{r}_0 - \mathbf{r}_i|^2}{2h_i^2}\right) \quad (\text{A2})$$

Accounting for the density gradient, the density profile along an arbitrary direction,  $\hat{n}$ , from this particle is then given by

$$\rho(s) = \rho|_0 + (\nabla\rho|_0 \cdot \hat{n})s, \quad (\text{A3})$$

where  $s = (\mathbf{r} - \mathbf{r}_0) \cdot \hat{n}$  and  $\rho|_0$  is the density at the position of the particle [ $\mathbf{r}_0$ ; eq. (A1)]. The optical depth at the particle’s position is computed by integrating the density profiles of contributing particles along the given direction. The correction to the optical depth caused

---

<sup>11</sup>The cubic spline kernel is well represented by a Gaussian with appropriate width. For ease of computation, we adopt the Gaussian-equivalent form for our post-processing calculations.

by the gradient near the particle’s position is obtained from integrating the gradient term in equation (A3) of the density profile. The correction to the optical depth is given by

$$\Delta\tau_{\hat{n}} = \int_0^{fh_0} (\nabla\rho|_0 \cdot \hat{n})/m_H\sigma dl, \quad (\text{A4})$$

where  $h_0$  is the smoothing length of the particle and  $f$  is a factor we can adjust to reflect where we truncate the integral. We take  $f = 2$  in our calculations, corresponding to truncating the integral at twice the particle smoothing length. Since we evaluate the gradient from discrete particle distributions, there are unavoidable numerical effects in the computed gradient, which can sometimes lead to corrections that are large and negative relative to the original optical depth. For these cases, we limit the corrected optical depth to be no less than 10% of the total optical depth. While these constitute only a small fraction of the total number of particles, they cannot be simply ignored because they typically lie at the transition region between optically thin and thick material.

We test our code on an SPH version of an isothermal sphere for varying resolutions and spatial configurations. We consider an isothermal sphere with a halo mass of  $10^{11}M_{\odot}$  (with a virial radius of 37.36 kpc). We consider two configurations: either the gas particles extend to the full virial radius or they only extend out to the inner 30% of the virial radius. The latter compact configuration may represent a case more akin to what we predict in cosmological hydrodynamic simulations. For each configuration we perform tests with three different mass resolutions by representing the gas with  $10^3$ ,  $10^4$  and  $10^5$  particles, respectively. We show the effect of this gradient as a function of geometry and resolution in Figure 20. The  $10^5$  particle case in which the particles are distributed to the full virial radius is shown in the far left panels of Figure 20. This case is shown to match the analytic predictions both for the neutral fraction profile (upper panels) and the surface brightness profile (lower panels). The reference analytic solution is computed for the singular isothermal sphere illuminated by the UVB by iteratively evaluating the attenuated UV intensity and solving the photo-ionization equilibrium equation at each radius (Zheng & Miralda-Escudé 2002b). The radial bin size is set to be sufficiently small to ensure an accurate solution. The surface brightness profile is obtained by gridding the particle emissivities on a regular  $256 \times 256$  grid. This is therefore a projected surface brightness profile, or a column emissivity as we discuss in the text.

Cosmological SPH simulations typically do not have many structures resolved this sharply. More commonly, structures will have one thousand to several tens of thousands of particles. To show the effect of low resolution, we show the neutral fraction and surface brightness profiles for this case represented by only 1000 particles in the middle panels of Figure 20. We see that the neutral fraction profile is reasonably well recovered when our gradient correction is included even at this low resolution (top middle panel). The bottom

middle panel of Figure 20 shows the surface brightness profile for this case. For the bulk of the sphere, the surface brightness is well recovered. However in the very center of the sphere, our calculation overpredicts the emissivity relative to the analytic case. This owes to the fact that the particle smoothing lengths are quite large in this case, and particles with large emissivities, centered at the transition between optically thick and thin gas, contribute emissivity formally in the center of the cloud where the neutral fraction approaches unity (and hence the emissivity approaches zero). The right panels in Figure 20 show the low-resolution ( $10^3$  particles) compact configuration case (particles distributed between the center of the cloud and 30% of the virial radius). The neutral fraction profile (top right) is recovered with large scatter. The surface brightness profile for this case is smoothed out relative to the  $10^5$  particle case. Here again, high emissivity particles are contributing flux at the center of the sphere owing to their large smoothing lengths and, similarly, the emissivity is diluted in the peak region owing to low emissivity particles.

The blue points in the top panels show the results of our calculation when we neglect the density gradient. Ignoring the density gradient results in significantly different neutral fraction profiles. While for very high optical depth (at the Lyman limit) and for very low optical depths the gradient is not important, at the transition region ( $1 < \tau_{LL} < 10$ ) the density gradients are quite large and play an important role. Because this region also produces and radiates the bulk of the Ly $\alpha$  emission, it is critical to get this region correct for fluorescence calculations. If we did not correct for the gradient, our peak surface brightness estimates would be in error (too low) by factors of 2, 3 and 5 in the  $10^5$ ,  $10^4$ , and  $10^3$  cases (for particles distributed to the virial radius). This would clearly have a major impact on our predictions. Therefore, even with the over-correction at the very center of these structures, it is far superior to the uncorrected case.

We further test our gradient correction in the presence of a bright ionizing source. While it is not feasible to analytically compute the UVB+QSO case, we can compute a “quasar only” case with our SPH sphere and compare the resultant surface brightnesses. For such a case, at each projected radius along the quasar-cloud direction, the calculation is reduced to a 1D problem and we use a method similar to Zheng & Miralda-Escudé (2002b) to obtain solution numerically. We use the same isothermal sphere configurations as in Figure 20, but we now irradiate these structures by our fiducial quasar. We show the results of this in Figure 21. Our gradient-corrected neutral density profile correctly recovers the surface brightness in this quasar illuminated case to better than a factor of two throughout the profile and particularly over the peak for these test configurations.

The SPH technique has natural limitations at boundaries with large density gradients and, for the purpose of fluorescence calculations, these boundaries are critical. We put forth

a technique to address this issue here that works with good but not perfect accuracy in the cases that we test. We adopt this method throughout the paper.

## B. Grid Convergence

To further assess the effects of grid resolution, we analyze a small sub-volume of the L5 simulation corresponding to just 65 kpc on a side. For the smallest smoothing lengths (0.07 kpc) in this simulation, this sub-volume resolves the minimum smoothing length with a grid of  $1024^3$ , which is manageable.

We first examine the effect of grid resolution on the projected emissivity distribution, i.e., the expected Ly $\alpha$  surface brightness if Ly $\alpha$  photons escaped without scattering. We note that the 2D resolution used for our Ly $\alpha$  and column emissivity images is always matched to the underlying 3D grid resolution we use to perform the scattering calculation. In the left panel of Figure 22 we plot the distribution of pixel emissivities projected on a  $64^2$ ,  $128^2$ ,  $300^2$ , and  $1024^2$  2D grid, which shows that our projected emissivity distribution is not sensitive to grid resolution and that the projected emissivity distribution converges for the  $64^2$  grid in this case. This suggests that typical sources are generally larger than 1kpc in size. To demonstrate convergence of our results for the pre-transfer emission for the full L5 region (1.5Mpc on a side), we show in the right hand panel of Figure 22 the pixel statistics for 2D Ly $\alpha$  emissivity with the  $64^2$ ,  $128^2$ ,  $300^2$ , and  $1024^2$  grid resolutions for the full region. The  $300^2$  grid converges with the  $1024^2$  grid, particularly at the high surface-brightness end, indicating a typical source size of  $\gtrsim 5$  kpc and we, therefore, feel comfortable adopting this resolution for our UVB-only computations. For the quasar-illuminated cases, the structures get smaller and we therefore go to a  $600^2$  grid to adequately recover the surface brightness distributions in this case.

The scattering process itself depends on how accurately the density, velocity and temperature distributions are rendered. To examine the robustness of our resulting Ly $\alpha$  images and spectra, we perform radiative transfer calculations for a region with a physical size of 150 kpc on a side gridded to a resolution of  $30^3$ ,  $100^3$  and  $300^3$  cells. Even the  $300^3$  grid does not resolve the smallest SPH smoothing length in this region. However, because gravitational forces are softened on scales of 0.48 kpc (for the spline kernel), the  $300^3$  grid should be sufficient to accurately capture the physical structure of the gas. Adopting a  $30^3$  grid for this region is equivalently coarse to using  $300^3$  for our main region of the L5 simulation of 1.5Mpc. In the upper left panel of Figure 23 we show this region and overlay several representative apertures from which we extract spectra. We compare the spectra for these apertures between the three resolutions in the remaining panels of Figure 23. We see from

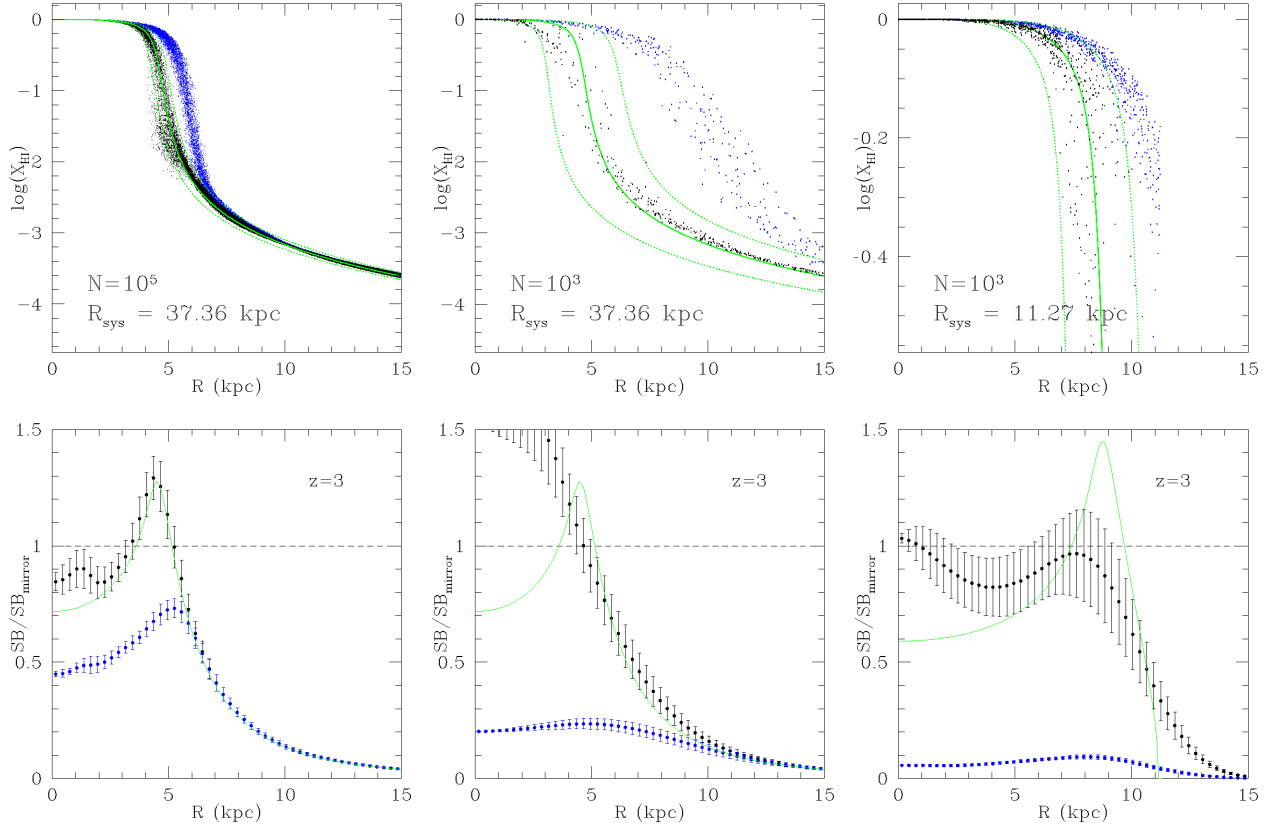


Fig. 20.— The effect of particle resolution and density gradient on the self-shielding solution. Top panels show the neutral fraction profiles for an SPH sphere with 100k particles (left), 1k particles (middle), and 1k particles (right). The left and middle panels have gas particles distributed within the entire virial radius of the halo in which the gas resides. The right panel has the particles arranged such that they only occupy the inner 30% of the virial radius. Bottom panels show the same configurations, but plot the surface brightness profiles without scattering (i.e. the column emissivity). Green solid lines in each panel show the exact solution, green dotted lines indicate the particle smoothing length, and black points show our solution. Blue points show the solution when the density gradient is neglected.



this figure that grid resolution does not play a large role in the resulting spectra as long as the cell size is  $\lesssim 5$  kpc; there are modest variations with resolution, but they do not systematically change the flux or spectral features. Similar conclusions hold for Ly $\alpha$  images (not shown). Based on this test, we adopt a grid resolution of  $300^3$  for the L5 simulations throughout our work for the UVB-only case. Since our L22 simulation has much coarser resolution (with a minimum spline-kernel softening length of 2.58 kpc), we conservatively adopt a grid resolution of  $300^3$  for calculations with this simulation. In the presence of a bright quasar, we adopt a  $600^3$  grid to ensure that grid resolution does not become an issue for the relatively smaller sources. We have tested that grid resolution higher than this leads to little change in the projected emissivity distribution for the high quasar luminosity we adopt.

### C. The Effect of Temperatures

A limitation for computing the Ly $\alpha$  emission from the simulations here is that the simulations are run assuming an omnipresent ionizing background (the optically thin approximation). Just as this background creates high ionization fractions in regions that would be self-shielded, those regions also have unrealistically high temperatures because of photoionization heating. The temperature differences themselves are moderate ( $1.5\text{--}2 \times 10^4\text{K}$  v.s.  $10^4\text{K}$ ), but they have an impact on collisional ionization rates and recombination rates, and hence on neutral fractions, and a large impact on collisional excitation rates, and hence on Ly $\alpha$  emissivity from cooling radiation. We present our method for correcting the simulation temperatures and the full prediction for cooling radiation (including collisional excitation as well as collisional ionization) in Paper II. The effect of the increased temperature is not only to change the emissivity of the gas in some regions, but also to decrease the neutral fractions in the gas. In this Appendix, we perform several tests to obtain a general idea about the effect of temperature change and collisional ionization on the *fluorescence* signature.

In general, the distribution of particles in the plane defined by the hydrogen number density and temperature in the simulation (the  $n_{\text{H}}\text{--}T$  plane) has three components (see KWH96 and Fig. 24): low-density gas that has been adiabatically cooled by cosmic expansion; overdense, shock-heated gas; and extremely overdense, radiatively cooled gas around  $10^4\text{K}$ . The low-density gas is likely to be exposed to the full ionizing background, so the optically thin approximation for background ionizing photons in the simulation is reasonable for this component. The temperatures of shock heated gas particles are not artificially high owing to the lack of self-shielding in the simulation, since photoionization alone cannot heat this gas to such high temperatures. In the  $n_{\text{H}}\text{--}T$  plane, the particles most affected by

the optically thin approximation are those with moderately high density and temperatures  $\sim 10^4\text{K} - 3 \times 10^4\text{K}$ . If self-shielding were correctly done in the simulation, these particles would be able to radiatively cool to  $10^4\text{K}$ .

Based on the above arguments, we define our fiducial model by applying a crude correction for the particle temperature: the temperatures of gas particles with high density ( $n_{\text{H}} > 10^{-3}\text{cm}^{-3}$ ) and low simulation temperature ( $T < 5 \times 10^4\text{K}$ ) are set to be  $10^4\text{K}$ , and the temperatures of all other particles are unaltered. The calculations presented in §4 and §5 are performed using this fiducial model.

To investigate the effect of temperature, we compare the results from the fiducial model (denoted as the “fidT” case) to those from two test cases. In the first test case (“simT” case), we simply adopt the particle temperatures as given by the simulation. In the other test case (“fixT” case), we set the temperatures of all particles to  $2 \times 10^4\text{K}$  as has been adopted by other authors (e.g., Cantalupo et al. 2005). In *all* cases, the neutral hydrogen fractions are computed assuming equilibrium between recombination and the sum of photoionization and collisional ionization, and the Ly $\alpha$  emissivity is computed as 66% of the photoionization rate (i.e., we are calculating only the fluorescent Ly $\alpha$  emission, not the Ly $\alpha$  cooling radiation). We choose the sub-region of the L5 simulation as in §4 to perform the comparison.

Figure 24 shows the probability distribution of particles in the  $n_{\text{H}}-T$  plane for the three cases. We divide the  $\log n_{\text{H}}-\log T$  space into a uniform grid. For each grid cell, we compute the total Ly $\alpha$  luminosity and the median neutral fraction from particles in that cell. The left panels show the luminosity distribution (the luminosity is arbitrarily normalized, but the normalization is the same for all cases), and the right panels show the neutral fraction distribution. The component of adiabatically cooled gas is not prominent in the plot, since we are zooming in on an overdense region. The top and middle panels compare the fidT and the simT cases. They look reassuringly similar. The fidT case lowers the temperature of particles that are likely to be artificially heated in the simulation. This change of temperature leads to an increase in the neutral fraction of these particles, as can be seen by comparing the right panels of the fidT and simT cases. Consequently, more of the gas can be self-shielded, which increases the effective area for intercepting ionizing photons and “reflecting” them back as Ly $\alpha$  photons. That is, the total fluorescent Ly $\alpha$  luminosity increases. However, the increase in the Ly $\alpha$  luminosity is small, which can be seen clearly from the comparison of the top and right histograms associated with the luminosity distribution panels for fidT and simT cases. The histograms show the Ly $\alpha$  luminosity distribution as a function of density and temperature. We also compare the post-transfer results for the two cases and again there is no large difference in Ly $\alpha$  images and spectra. Therefore, our fiducial case and the case adopting the simulation temperature are similar to each other for fluorescent Ly $\alpha$  emission.

A comparison between the fidT (top panels) and the fixT (bottom panels) cases shows that adopting a fixed particle temperature of  $2 \times 10^4\text{K}$  has a dramatic impact on both the neutral fraction and luminosity distributions of particles. The effect is primarily on the shock-heated gas. While this diffuse gas is largely optically thin and contributes little to the Ly $\alpha$  emissivity in the fidT case, reducing the temperature as in the fixT case leads to significant shielding effects for some fraction of this gas in dense regions. This can be clearly seen in Figure 24 by comparing the neutral fraction distributions of the fidT and fixT cases. Because of the large spatial extent of the shock-heated gas, the artificial shielding caused by lowering the temperatures greatly increases the effective area for “reflecting” ionizing photons. Therefore, we see a substantial increase in the Ly $\alpha$  luminosity caused by shock-heated gas (see the histograms in the bottom-left panel), which is physically implausible.

As a consequence of the differences in the Ly $\alpha$  luminosity and neutral hydrogen fraction distributions, the Ly $\alpha$  images and spectra from the fixT case and the fidT (or simT) case are dramatically different as shown in Figure 25. Fixing the temperature to  $2 \times 10^4\text{K}$  significantly alters the morphology of the Ly $\alpha$  emission. The image from the fixT case shows far more extended Ly $\alpha$  emission, giving the impression of a single large structure of emitting gas. Adopting more realistic temperatures correctly removes the contribution of moderately dense but shock-heated gas from the emission signal. As a result, we are left with emission from denser, compact knots of material, seen in the image of the simT case. The 2D spectra in the right panels also reflect this morphological change – the spectra are far more diffuse in the fixT case, as the fixed (low) temperatures increase the neutral column densities of structures with respect to the fidT/simT cases. This highlights the necessity of having accurate simulation temperatures when computing Ly $\alpha$  emission for comparison with future observations. Since simulations with a fully self-consistent self-shielding correction are not available, our approach is acceptable in that we compute the neutral fractions by making reasonable corrections to gas temperatures rather than adopting either simulation temperatures or fixing the temperature to a constant value. We note however, that total Ly $\alpha$  emission (including cooling radiation) is much more sensitive to the differences between SimT and FidT than is the fluorescent emission. Hence, the temperature treatment is extremely important when predicting total Ly $\alpha$  fluxes for comparison with observations.

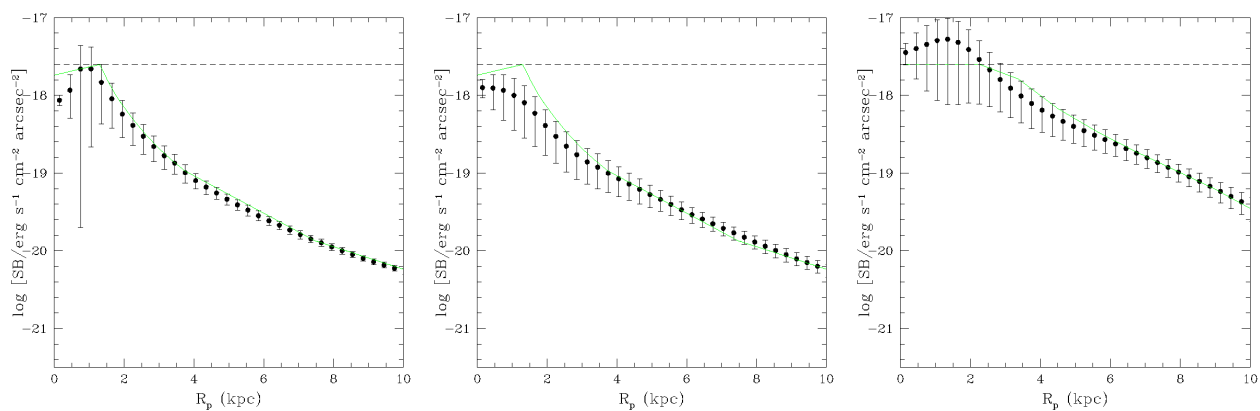


Fig. 21.— The recovery of a quasar only radial surface brightness profile for the three cloud configurations and resolutions shown in the lower panels of Figure 20. Blue points show the analytic case, black points show the dispersion of surface brightness pixels in a 2D map of the  $\text{Ly}\alpha$  column emissivity and green points show the mean value of the black points. The dashed horizontal line shows the “mirror” expectation for this case. The gradient-corrected quasar case recovers the true surface brightness distribution to better than a factor of three throughout even at low resolution.

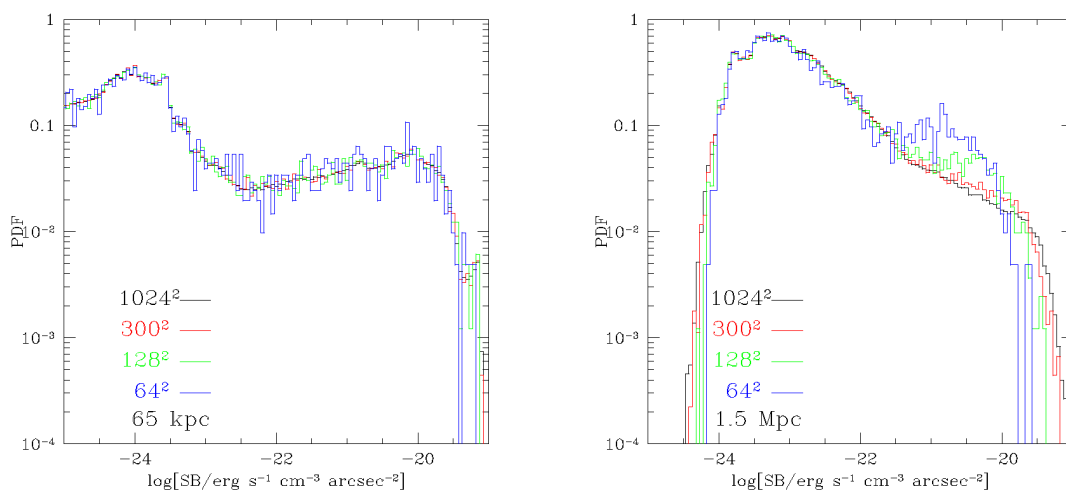


Fig. 22.— Distribution of projected emissivity of pixels as a function of grid resolution. The left panel shows convergence for a cubic sub-region simulation of 65 kpc (physical) on a side at  $z = 3$ . The projected emissivity distribution converges even with a  $64^2$  grid, which corresponds to a pixel size of  $\sim 1$  kpc on a side. The right panel shows the distribution of 2D emissivity for the fiducial 1.5 Mpc (physical) region. The  $300^2$  grid (corresponding to a cell size of  $\sim 5$  kpc on a side) reaches convergence, and we therefore adopt this for our Ly $\alpha$  radiative transfer calculations.

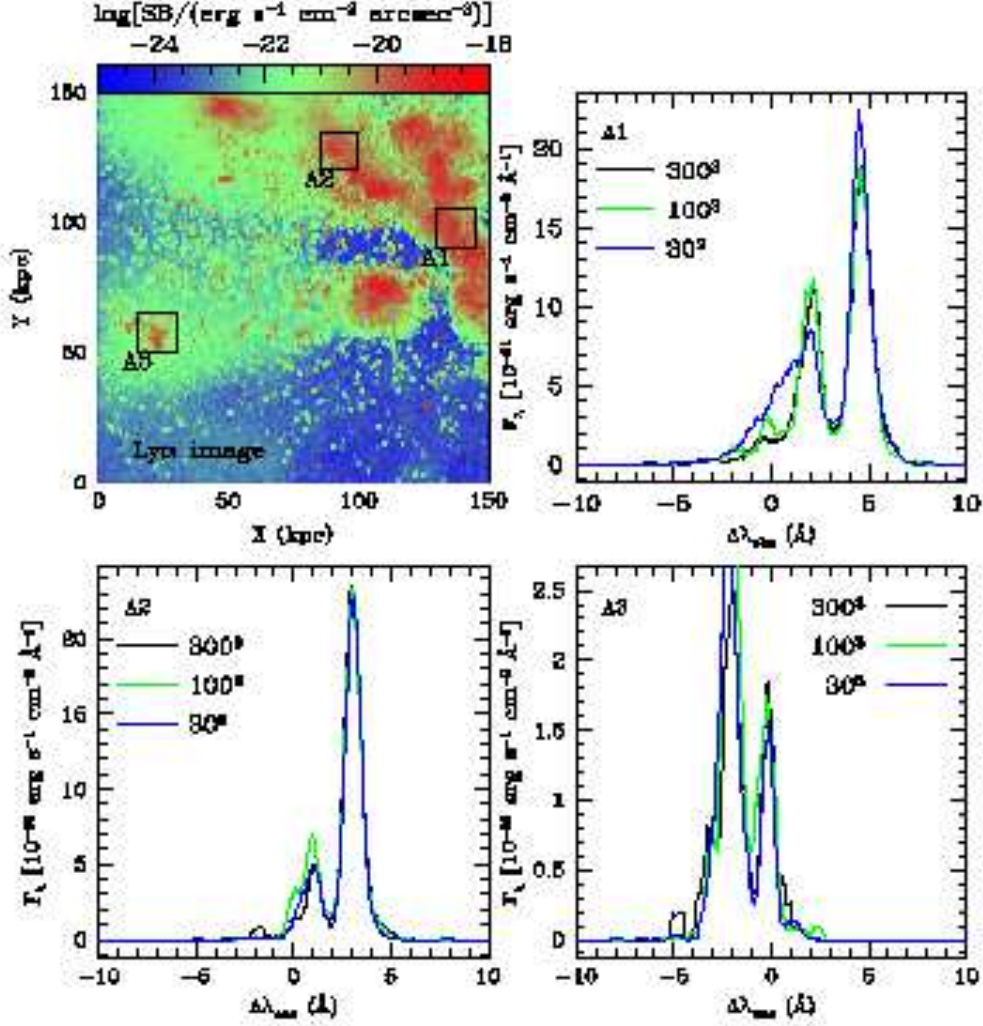


Fig. 23.— Convergence of the 1D spectra in a 150 kpc region of the L5 simulations. The upper left panel shows the apertures overlaid on the Ly $\alpha$  image. Remaining panels show the 1D spectra from these apertures as a function of grid resolution. From the figure, we see that the  $30^3$  grid recovers the true 1D spectrum well from this small sub-region of the simulation. This is analogous to using a  $300^3$  grid on the larger portion of the L5 simulation from which we obtain the results presented in this paper.

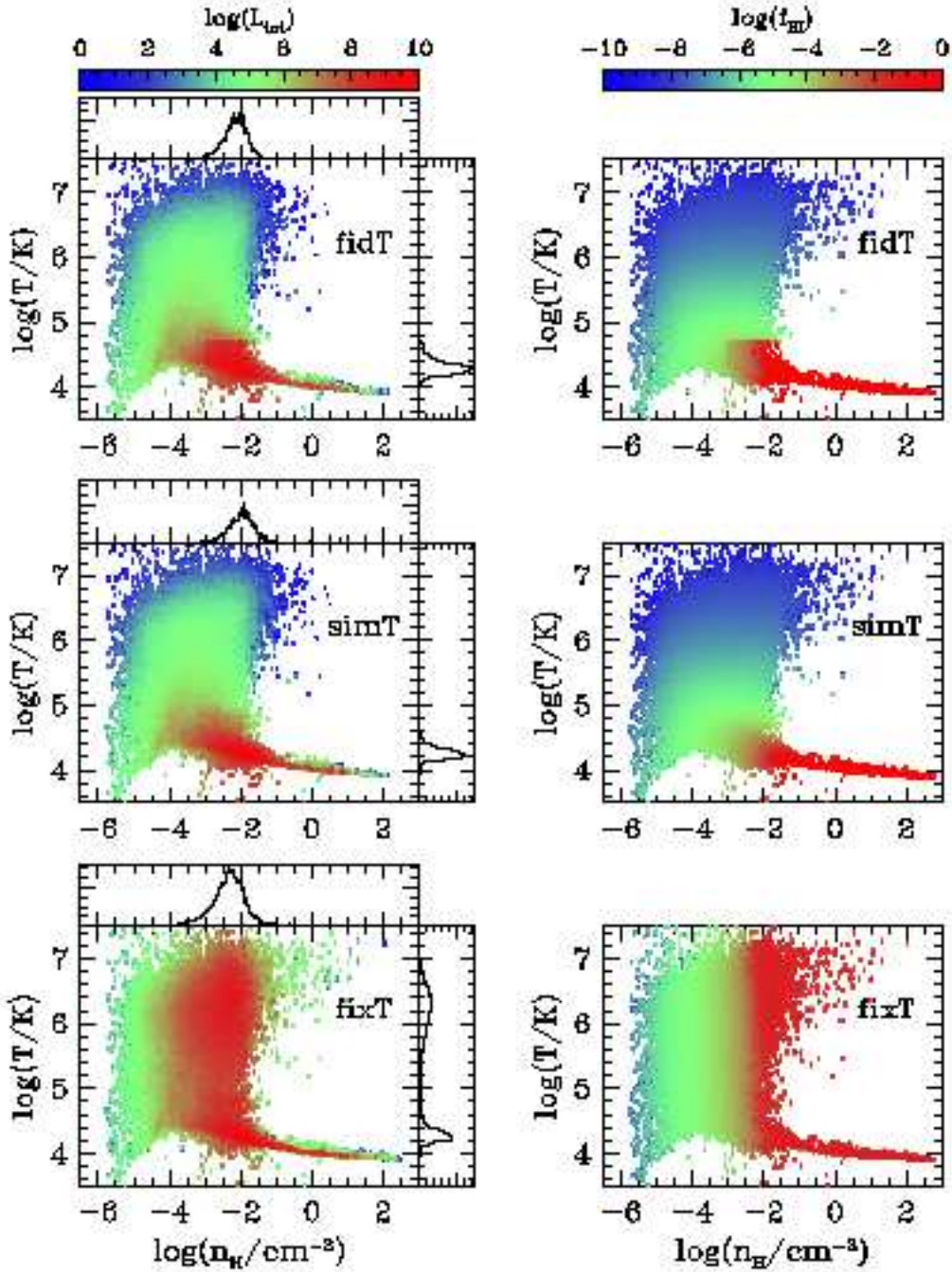


Fig. 24.— Distribution of particle luminosity (*left*) and neutral fraction (*right*) in the temperature-density plane for particles in the sub-region of the L5 simulation. Top panels show our fiducial case (fidT). Middle panels show the case in which simulation temperatures are adopted directly (simT). Bottom panels show the case in which particles are set to a constant temperature of  $T = 2 \times 10^4$  K (fixT). The histograms associated with the left panels show the luminosity distribution as a function of particle density (top histogram) and temperature (right histogram).

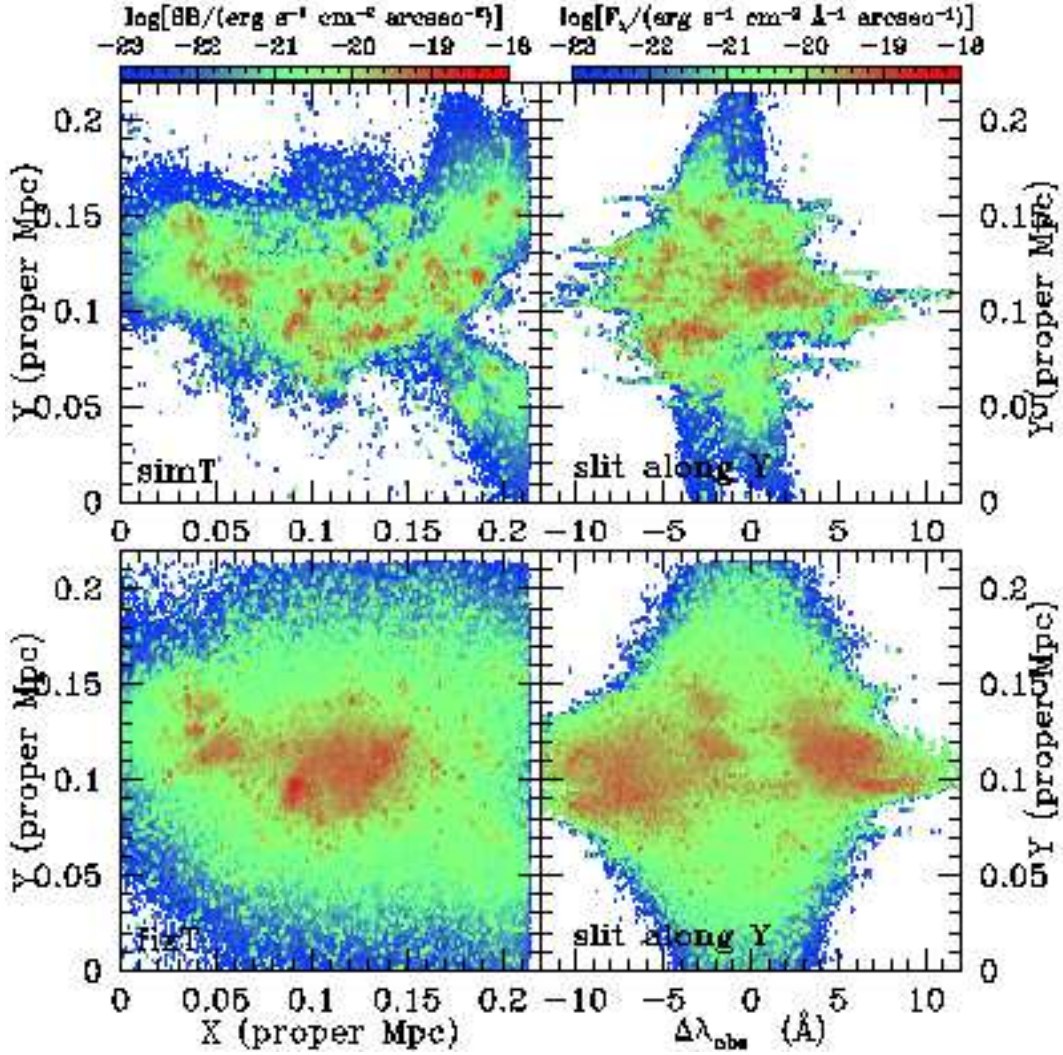


Fig. 25.— Comparison of Ly $\alpha$  fluorescence from the sub-region of the L5 simulation when the simulation temperatures are adopted (simT, top panels)) and when the gas temperature is fixed at  $2 \times 10^4\text{K}$  (fixT, bottom panels). The results of the simT case are similar to our fiducial model shown in Figure 9. The striking differences in morphology and emissivity directly result from the false shielding effect of shocked gas when the temperatures are artificially lowered to  $2 \times 10^4\text{K}$ .